Conformation control of the histidine kinase BceS of *Bacillus subtilis* by its cognate ABC-transporter facilitates need-based activation of antibiotic resistance

Alan Koh[1,2], Marjorie J. Gibbon[1,2], Marc W. Van der Kamp[3], Christopher R. Pudney[1], Susanne Gebhard[1,2]*

[1]Department of Biology and Biochemistry, [2]Milner Centre for Evolution, University of Bath, Claverton Down, Bath, BA2 7AY, United Kingdom; [3]School of Biochemistry, University of Bristol, University Walk, Bristol, BS8 1TD, United Kingdom.

*Corresponding author. Phone: +44 1225 386421; E-mail: s.gebhard@bath.ac.uk;

Running title: Kinase control by an ABC-transporter

Keywords: Signal transduction, flux-sensing, antimicrobial peptide, cell envelope stress

Data accessibility statement: The data that support the findings of this study are available from the corresponding author upon reasonable request.

SUMMARY

Bacteria closely control gene expression to ensure optimal physiological responses to their environment. Such careful gene expression can minimize the fitness cost associated with antibiotic resistance. We previously described a novel regulatory logic in *Bacillus subtilis* enabling the cell to directly monitor its need for detoxification. This cost-effective strategy is achieved via a two-component regulatory system (BceRS) working in a sensory complex with an ABC-transporter (BceAB), together acting as a flux-sensor where signaling is proportional to transport activity. How this is realized at the molecular level has remained unknown. Using experimentation and computation we here show that the histidine kinase is activated by piston-like displacements in the membrane, which are converted to helical rotations in the catalytic core via an intervening HAMP-like domain. Intriguingly, the transporter was not only required for kinase activation, but also to actively maintain the kinase in its inactive state in the absence of antibiotics. Such coupling of kinase activity to that of the transporter ensures the complete control required for transport flux-dependent signaling. Moreover, we show that the transporter likely conserves energy by signaling with sub-maximal sensitivity. These results provide the first mechanistic insights into transport flux-dependent signaling, a unique strategy for energy-efficient decision making.

36 **INTRODUCTION**

37 Bacteria have exquisite abilities to respond to environmental conditions carefully balancing
38 the benefits of a response against the associated metabolic cost. The importance of this is
39 particularly evident in the context of antibiotic resistance, where one of the main
40 counteracting forces working against the development and spread of resistance is the
41 associated cost in fitness (Andersson and Hughes, 2010; Waglechner and Wright, 2017;
42 Durão *et al.*, 2018). To minimize this cost, many resistance determinants are tightly
43 regulated, which requires that the bacterium is able to accurately determine the severity of an
44 antibiotic attack and adjust gene expression accordingly. We previously described a new
45 sensory strategy in *Bacillus subtilis* that produces an exquisitely fine-tuned response, with
46 three orders of magnitude of output modulation over an input dynamic range of three orders
47 of magnitude (Fritz *et al.*, 2015). This regulatory logic is achieved by a two-component
48 system (BceRS) whose histidine kinase, BceS, works in a sensory complex with an ABC-
49 transporter, BceAB (Dintner *et al.*, 2014; Fritz *et al.*, 2015) (Fig. 1). BceRS controls
50 expression of the *bceAB* operon, and the resulting increased production of the transporter
51 provides resistance against the peptide antibiotic bacitracin (Ohki *et al.*, 2003). A defining
52 characteristic of this system is that the histidine kinase lacks any apparent sensory domains
53 and instead requires the transporter for activation in response to bacitracin (Rietkötter *et al.*,
54 2008; Hiron *et al.*, 2011).

55 Such systems are wide-spread among low G+C content Gram-positive bacteria, including
56 bacilli, lactobacilli, staphylococci, streptococci, enterococci and clostridia (Ouyang *et al.*,
57 2010; Staroń *et al.*, 2011; Hiron *et al.*, 2011; Dintner *et al.*, 2011; Revilla-Guarinos *et al.*,
58 2013; Gebhard *et al.*, 2014). They are collectively referred to as Bce-like systems and impart
59 resistance against a broad range of cell wall-active peptide antibiotics (Gebhard and Mascher,

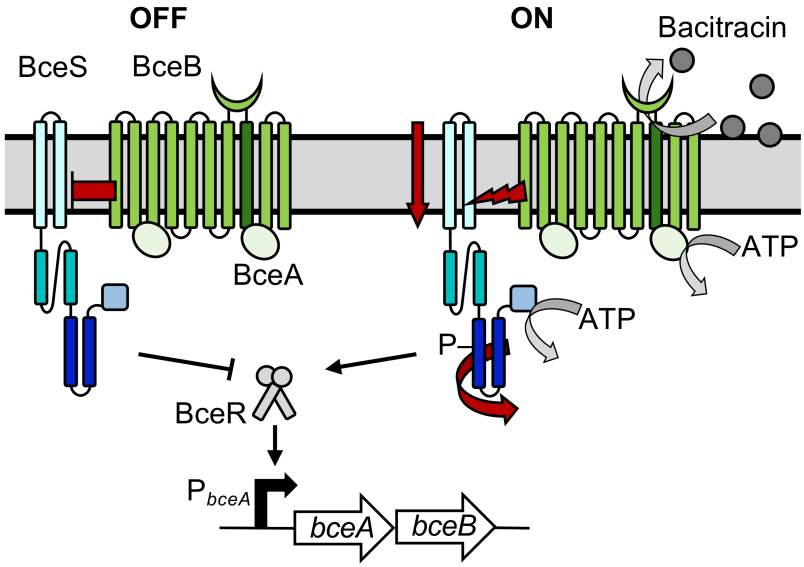

Figure 1. Function of the BceRS-BceAB resistance system of *B. subtilis*. BceS and its domains are shown in shades of blue, with the HAMP-like domain in dark turquoise, and DHp domain in dark blue. Only a single monomer of BceS is shown for clarity. The BceB permease is in bright green with the 8th transmembrane helix marked in dark green and the extracellular domain indicated by a green crescent; two molecules of the ATPase BceA are shown in pale green associated with the BceB monomer, according to the A2B stoichiometry (Dintner *et al*., 2014). The left section of the schematic shows the system in its inactive (OFF) state, and the repressing function of the transporter indicated by a red blunt arrow. The right shows the active (ON) state in the presence of antibiotics, exemplified by bacitracin, with the activating function of the transporter shown as a red lightning bolt. The motions of kinase domains upon activation are shown as red block arrows and BceS autophosphorylation by a 'P'. The positioning of the symbols within the sensory complex for repression/activation is arbitrary. ATP hydrolysis reactions and antibiotic removal are indicated by grey arrows; for simplicity ATP hydrolysis is only shown for one ATPase.

60 2011; Revilla-Guarinos *et al.*, 2014). Based on computational modelling of the response
61 dynamics in the *B. subtilis* Bce system, we have established that signaling is proportional to
62 transport activity (Fritz *et al.*, 2015). Because the transporter mediates the actual resistance,
63 presumably by removal of the antibiotic from its target in the cell envelope (Gebhard, 2012;
64 Fritz *et al.*, 2015; Greene *et al.*, 2018; Kobras *et al.*, 2020), increased transporter production
65 acts a negative feedback on signaling, which creates the characteristic gradual, fine-tuned
66 response (Fritz *et al.*, 2015). This flux-sensing mechanism effectively allows the bacterium to
67 adjust its response according to its need for additional detoxification capacity, implementing
68 a cost-effective 'produce-to-demand' strategy. However, the molecular mechanism of this
69 new signaling strategy, i.e. how the activity of the histidine kinase is controlled within the
70 sensory complex and how this creates the observed analog response behavior, remains
71 unknown.

72 Histidine kinases typically relay extracellular information to the cytoplasm via
73 autophosphorylation at a conserved histidine residue, which then leads to phosphorylation of
74 a cytoplasmic response regulator that elicits changes in gene expression (Gao and Stock,
75 2009). Despite their importance in bacterial signaling, we still have limited understanding of
76 the molecular mechanisms by which histidine kinases transmit information through the
77 cytoplasmic membrane. This is in part due to the modular architecture of the kinases, which
78 allows a plethora of different input domains to be coupled to a conserved catalytic core. The
79 core consists of a DHp (also known as HisKA) domain that facilitates dimerization and
80 histidine phosphotransfer, and a C-terminal ATPase domain (Gao and Stock, 2009). The
81 extracellular input and cytoplasmic core domains are separated by transmembrane segments
82 and usually at least one cytoplasmic signal transfer domain (e.g. HAMP or PAS domains)
83 (Gao and Stock, 2009; Gushchin *et al.*, 2017). Recent studies of histidine kinase domains in
84 isolation or together with an adjacent domain suggest that transmembrane signaling can occur

85 via rotating and scissoring motions and piston-like helical displacements of transmembrane
86 helices (Bhate, Molnar, Goulian, and DeGrado, 2015a; Monzel and Unden, 2015; Gushchin
87 *et al.*, 2017; Bhate *et al.*, 2018). The nature of transmembrane motions largely appears to
88 depend on their context with sensory and signal transfer domains, although the individual
89 motions are not mutually exclusive (Gushchin and Gordeliy, 2017; Jacob-Dubuisson *et al.*,
90 2018).

91 Additionally, several kinases are controlled by accessory proteins. In many cases, these
92 accessory proteins are transporters (Tetsch and Jung, 2009; Piepenbreier *et al.*, 2017), and
93 most act as repressors of kinase activity, with deletion of the transporter causing constitutive
94 activation of signaling (Hsieh and Wanner, 2010; Witan *et al.*, 2012; Unden *et al.*, 2016). The
95 flux-sensing Bce-like systems are unique in that the histidine kinases fully rely on their
96 cognate transporters for activation, and remain inactive when the transporter is deleted
97 (Rietkötter *et al.*, 2008; Gebhard and Mascher, 2011). Moreover, implementing the reported
98 flux-sensing strategy requires kinase activity to be directly proportional to transport activity
99 (Fritz *et al.*, 2015). To our knowledge, no information is available on how accessory proteins
100 may achieve such positive and precise control over a histidine kinase.

101 In the present study, we sought to understand the mechanistic basis of histidine kinase
102 activation in the Bce system of *Bacillus subtilis* and how this links to the system's analog
103 signaling behavior. Through computational predictions, detailed mutagenesis and cysteine
104 cross-linking and accessibility analyses, we provide evidence that the kinase BceS is
105 activated via helical rotations in the DHp domain, accompanied by a piston movement in the
106 second transmembrane domain. Physical motions are most likely relayed via a poorly
107 conserved intervening HAMP-like domain. We also show that the transporter not only acts as
108 the activator of the kinase, but also controls its inactive state. We propose it is this complete

109 control over kinase conformation that couples its activity to that of the transporter.
110 Surprisingly, mutagenesis of the putative signaling domain of the transporter, BceAB,
111 highlighted that the system has not evolved for maximal signaling sensitivity, which likely
112 represents an additional layer of fine-tuning and energy conservation.

113

114 **RESULTS**

115 **Generation and validation of a BceS homology model.** Analysis of the domain architecture
116 of BceS using SMART (Letunic *et al.*, 2012) showed two N-terminal transmembrane helices,
117 predicted to end at residue F55, and a prototypical cytoplasmic kinase core with a DHp
118 domain from residues E115 to I172 and ATPase domain from S216 to N326. The 60 amino
119 acid linker between the transmembrane and DHp domains contained no predicted domains.
120 To investigate the cytoplasmic composition of BceS in more detail, we used I-TASSER
121 (Zhang, 2008) to predict the tertiary structure of the linker region and DHp domain (residues
122 R56 to N174; Fig. 2a). The closest structural analog was a hybrid protein consisting of the
123 HAMP domain of Af1503^{A291V} from *Archaeoglobus fulgidus* and the DHp domain of *E. coli*
124 EnvZ (PDB 3ZRW; see methods for quality scores), which shares 20% sequence identity and
125 40% similarity with the BceS fragment used for structure prediction. The homology model of
126 BceS showed the typical DHp domain fold of two antiparallel helices (DHp1 and DHp2),
127 joined by a short loop. In the functional kinase dimer, this will form the four-helix bundle
128 characteristic for most histidine kinases (Gao and Stock, 2009) (Fig.2c). Interestingly, the
129 linker between the membrane interface and DHp domain adopted a HAMP-like conformation
130 with two short parallel helices (HAMP-like 1 and HAMP-like 2), where HAMP-like 2
131 continues into DHp1 as a single continuous helix (Fig. 2a). The relevance of this domain,
132 which had not been predicted in previous analyses (Mascher, 2006; Dintner *et al.*, 2011), is

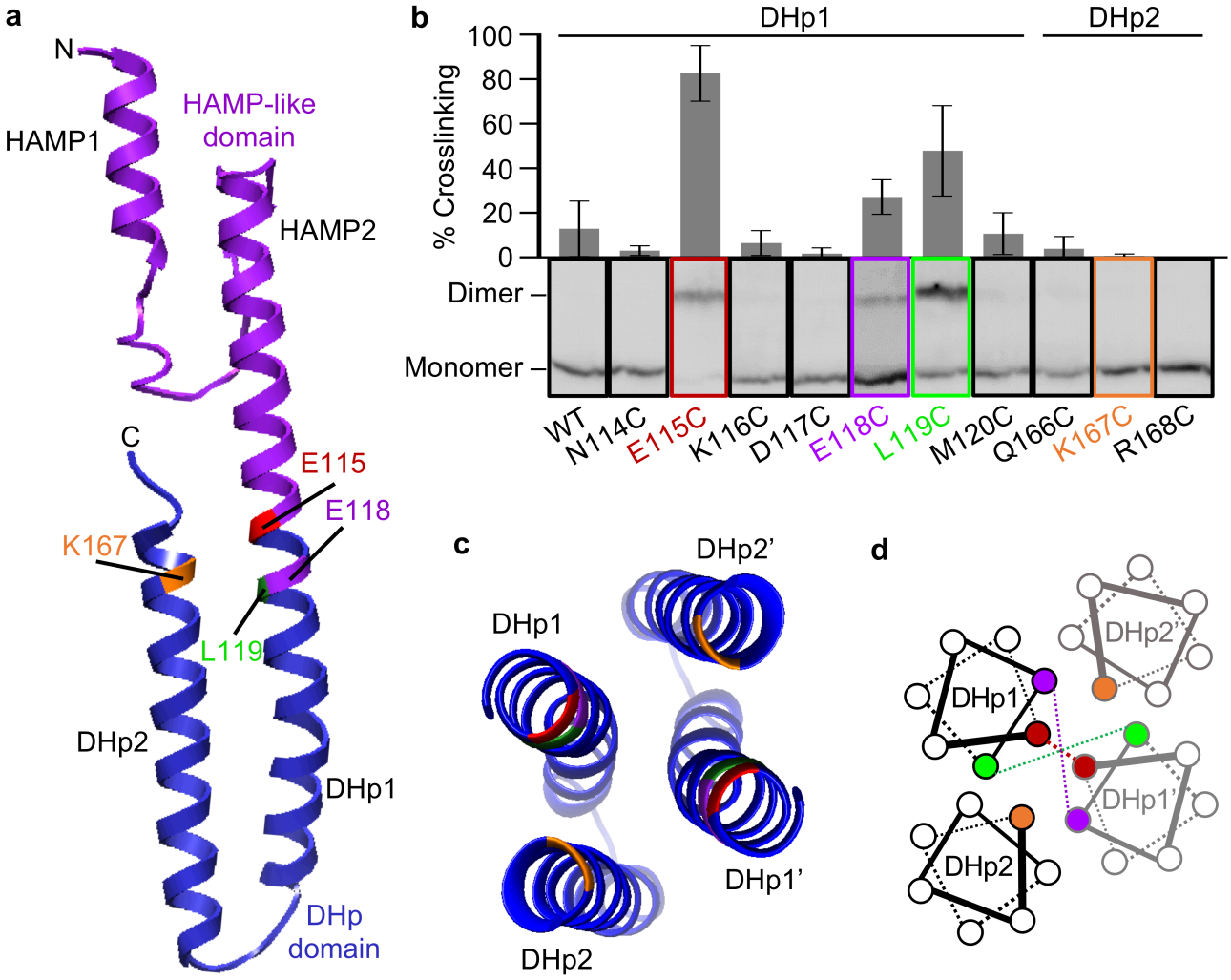

Figure 2: BceS DHp domain forms a four-helix bundle. a, Homology model of the BceS HAMP-like and DHp domains generated by I-TASSER (C-score = -0.76). The HAMP-like domain is shown in purple and the DHp domain in blue. The residues that form Cys-crosslinks in panel b are highlighted, E115 (red), E118 (purple) and L119 (green). Residue K167, which sits opposite E115, is shown in orange. b, Percentage of crosslinking for each BceS Cys variant was calculated from relative band intensities between monomer and dimer within each lane using Fiji (Schindelin et al., 2012). Amino acid substitutions were introduced in parent construct bceSWT-His8 (SGB369) and BceS production was controlled by addition of 0.02 % (w/v) xylose. Data are shown as mean ± SD from 2-5 independent repeats. c, d, Schematic diagram of the BceS DHp dimer configuration. Helices labelled DHp1' and DHp2' show the second protomer. Left, top down view of the helices in the structural model; right, helical wheel diagram of the top two helical turns in the DHp domain; residues that form crosslinks are highlighted as before.

133 discussed in more detail below. It should be noted that confidence in the exact conformation
134 of the loops linking the two helices in the HAMP-like domain, and the short loop linking the
135 two DHp domain helices is low in the homology model due to the presence of Ramachandran
136 outliers (see Methods). However, the overall model still provided a plausible illustration of
137 the BceS structure and was used to inform further experimental design.

138 To test the accuracy of the homology model, we probed the relative orientation of helices
139 within the DHp domain four-helix bundle, based on proximity of individual residues, using
140 oxidative cysteine crosslinking. These experiments were done *in vivo* using cells deleted for
141 the native copy of *bceS* and carrying a single-copy ectopic construct for expression of *bceS*
142 with a C-terminal His_8-tag, allowing slight over-production of the kinase to facilitate
143 detection by Western blot analysis. BceS contains three native Cys residues, C45 in the
144 second transmembrane helix and C198 and C259 in the ATPase domain. Based on their
145 physical distance from each other and the DHp domain, we did not expect these residues to
146 interfere with our analysis, and indeed no crosslinking product was observed upon oxidation
147 with iodine in wild-type BceS (Fig. 2b). Next, single cysteine substitutions were introduced
148 in the first two helical turns of the helix DHp1 (N114 to M120), and in equivalent positions
149 near the end of the helix DHp2 (Q166 to R168). Disulfide bond formation in these variants
150 should only occur if the substituted residues come into close proximity in the kinase dimer
151 (Pakula and Simon, 1992). The only residues that consistently formed detectable crosslinks
152 were at positions 115, 118 and 119, with the highest degree of crosslinking at position 115
153 (Fig. 2b). This is in good agreement with their positioning at the core of the four-helix bundle
154 and shows that the structural model closely reflects the conformation of BceS in the cell (Fig.
155 2c).

156 To ensure that the introduction of cysteines had not affected the integrity of the protein, we
157 tested the activity of each BceS variant *in vivo*. This was based on their ability to induce
158 expression from the system's target promoter fused to a reporter gene (P_{bceA}-*luxABCDE* or
159 P_{bceA}-*lacZ*), following exposure to the antibiotic bacitracin (Fritz *et al.*, 2015). Only the
160 K116C and K167C substitutions led to a complete loss of activity (Fig. S1a). It is therefore
161 possible that the lack of crosslinking observed for the latter, which also faces the core of the
162 DHp domain (Fig. 2c), could be explained by defects in the protein rather than the distance
163 between DHp2 helices in the kinase dimer.

164 **Charge substitutions in the DHp core suggest a rotation mechanism of kinase**
165 **activation.** Inspection of the DHp domain revealed a striking concentration of charged
166 residues at the membrane-proximal end of the four-helix bundle (Fig. 3). In the wild-type
167 kinase, E115 and K167 create a net neutral charge in the bundle core. As described above and
168 previously (Fritz *et al.*, 2015), cells harbouring wild-type BceS strongly activate expression
169 of the P_{bceA}-*lux* reporter in the presence of bacitracin, while in the absence of the antibiotic
170 the activity of the reporter is below the detection limit (Fig. 3a, WT). Interestingly, creation
171 of an 'all negative' (K167D substitution) or 'all positive' (E115K substitution) DHp core
172 resulted in a strong increase in the basal level of the kinase, while the activity in the presence
173 of the inducer remained unaffected (Fig. 3a). To test whether this effect was indeed due to the
174 changes in core charge and not to substitutions at this position *per se*, we introduced a series
175 of other amino acids into position 115. Exchanging E115 for a different positively charged
176 amino acid, Arg, again resulted in an increase in basal activity, although less pronounced
177 (Fig. S1c). Substitution for Ala or Cys had no detectable effect on activity, showing that the
178 presence of charged amino acids was not in itself important for kinase function. This is
179 consistent with the high density of charged residues in this part of BceS not being conserved
180 among its homologues ((Dintner *et al.*, 2011) and data not shown). Moreover, the constitutive

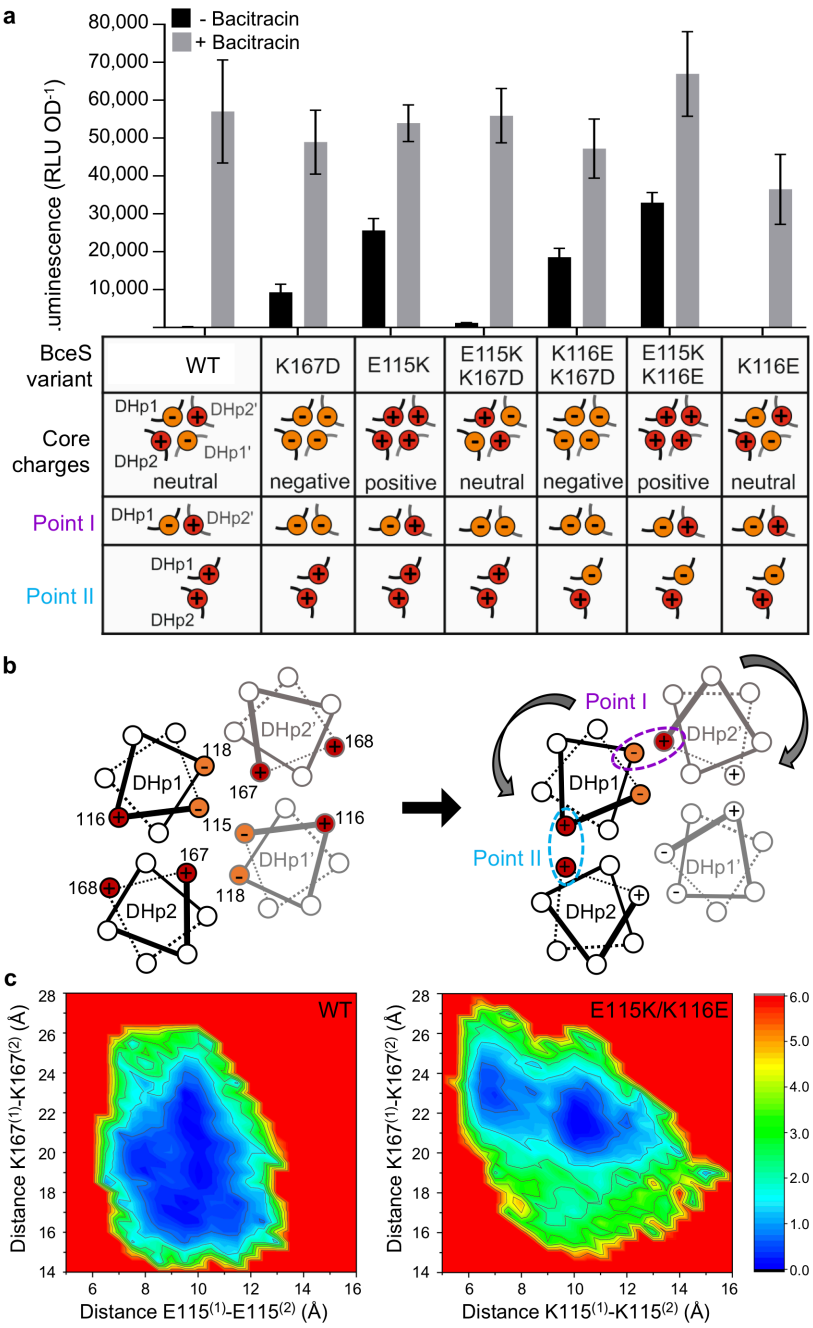

Figure 3: Charges within the BceS DHp domain core affect kinase activity. a, BceS signaling activity in strains harbouring PbceA-luxABCDE and Pxyl-bceS. Amino acid substitutions were introduced in parent construct bceSWT-His8 (SGB369). Signaling was induced with 1µg ml-1 of bacitracin. Data are shown as mean ± SD from 4-22 biological repeats. The schematic below shows the location of individual and net charges in the core and stabilisation points within the four-helix bundle, as illustrated in panel b. Red, positive charge; orange, negative charge. Unpaired t-test comparison to WT showed significant differences ($p<0.0001$) in the absence of bacitracin for all variants except K116E ($p=0.8$), and no significant differences ($p>0.1$) in the presence of bacitracin for all variants, except K116E ($p=0.04$). Differences with vs without bacitracin were significant ($p<0.005$) in all strains. b, Helical wheel diagram of the top two helical turns in the DHp dimer configuration showing location of charges and stabilisation points (pink and cyan). Helices labelled DHp1' and DHp2' show the second protomer. Grey curved arrows denote the direction of helical rotation. For orientation, the distance between residues at position 115 is likely to be in the range of 4-12 Å based on our cysteine cross-linking results. c, 2D plots of potential of mean force (PMF) obtained in GaMD simulations of the wild type (WT, left) and E115K/K116E variant (right) protein. Inter-monomer distances shown are between the Cα carbon atoms of residues at positions 115 (x-axes) and 167 (y-axes). The PMFs are projected onto the surface in kcal mol−1 indicated by the heat scale.

181 kinase activity could be returned to near wild-type levels by restoring the net neutral charge
182 through combining the E115K and K167D substitutions (Fig. 3a). We therefore concluded
183 that the high constitutive activity in the absence of the inducer was indeed due to the presence
184 of four residues with the same charge in the DHp domain core.

185 In the current model for histidine kinase activation, the DHp domain undergoes a helical
186 rotation (Gushchin *et al.*, 2017). The strong activating effect we observed upon introduction
187 of four residues of the same charge at the core of the domain made it tempting to speculate
188 that charge repulsion may force BceS to undergo such a rotating motion, placing it in its
189 activated state. According to our homology model, rotation of the helix DHp1 in a counter-
190 clockwise direction and DHp2 in clockwise should create two new points of contact between
191 charged residues: point I between E118 and K167, and point II between K116 and R168 (Fig.
192 3b). The opposing charges in point I should have a stabilizing effect on the rotated state, and
193 removing this in the K167D variant may explain its lower basal activity compared to E115K
194 (Fig. 3a). In contrast, the proximity of two positive charges in point II should have a de-
195 stabilizing effect. Replacing one of these with a negative charge (K116E) by itself had no
196 effect on kinase activity. However, combining K116E with the activating effect of the E115K
197 substitution led to a further increase of basal kinase activity compared to E115K alone (Fig.
198 3a). This effect is entirely consistent with kinase activation through helical rotations in the
199 DHp domain, where we could achieve the highest artificial activation of the protein through
200 creating charge repulsion in the kinase core, while stabilizing the rotated state through
201 opposing charges in the two new points of contact.

202 Attempts were made to detect this DHp domain rotation *in vivo* using cysteine crosslinking,
203 either following induction with bacitracin or using the constitutively active E115K/K116E
204 variant. No quantitative conclusions could be drawn, however, due to the very large

205 experimental errors (Fig. S2). To provide further evidence of conformational change in the
206 DHp domain, we turned to molecular dynamics (MD) simulations. As discussed above, the
207 homology model (Fig. 2) shows excellent agreement with experimental validation, indicating
208 that it is a reasonable starting point for MD simulations. Given the relatively large putative
209 rotation, we applied Gaussian accelerated MD (GaMD) to more completely sample
210 conformational space (Miao *et al.*, 2015).

211 To assess conformational differences in the DHp domain between the wild-type kinase and
212 the constitutively active E115K/K116E variant, GaMD simulations were performed on both
213 for a total of 2 μs each (four replicas of 500 ns; Figure S3a). From our simulations, we
214 calculated the potential of mean force (PMF) for a series of internuclear distances for both
215 wild-type and variant residues, to serve as a proxy for the energetic barrier between
216 conformational sub-states. To best illustrate the relative orientation of helices in the DHp
217 domain bundle, we focused on positions 115 and 167, facing the bundle core (Fig. 3). The
218 PMF plots for the internuclear pairs of these residues between monomeric units of the DHp
219 domain are shown in Figure 3c. The lower the PMF value, the more likely the helices will
220 occupy the conformational state defined by the internuclear distances shown. In the wild-type
221 DHp domain, the PMF plot for distances between monomers at amino acids 115 and 167
222 shows a broad minimum across most of conformational space (Fig. 3c, left). This suggest that
223 there is a relatively high propensity for the domain to explore a diversity of conformational
224 space. Figure 3c (right) shows the same data for the variant DHp, which, instead of the broad
225 minimum, now shows two distinct, more restricted minima. More specifically, the tendency
226 towards a longer K167 distance in the variant would seem consistent with our model for helix
227 rotation (Figure 3b). To more clearly explore the differences between conformational space
228 accessed, we performed principal components analysis (PCA) of the data from Figure 3c.
229 This indicates that there is a significant difference in the principal component space sampled

230 (Fig. S3b), meaning the variant DHp occupies a conformational space that is not accessible to
231 the wild-type domain. Based on the high constitutive activity of the variant, it is plausible to
232 assume that this new conformational space represents the active state of the kinase.
233 Importantly, our simulations show that the wild-type kinase is unable to adopt this
234 conformation on the simulated time scales. This is consistent with our *in vivo* data that shows
235 no detectable kinase activity without activation through the transporter.

236 **BceS contains a HAMP-like signal transfer domain.** Contrary to previous predictions
237 (Mascher, 2006; Dintner *et al.*, 2011), the BceS homology model showed a domain with
238 structural similarity to a HAMP domain between the second transmembrane helix and the
239 DHp domain. HAMP domains adopt a parallel four-helix bundle arrangement with two
240 alternative states of helix packing that transmit a conformational change from an upstream
241 input to a downstream output domain by turning various input movements consistently into
242 helical rotation (Hulko *et al.*, 2006; Lai and Parkinson, 2014; Gushchin *et al.*, 2017). The
243 four-helix bundle is stabilized through multiple packing layers, predominantly mediated by
244 hydrophobic residues (Hulko *et al.*, 2006; Zhou *et al.*, 2011). A sequence alignment of known
245 HAMP domains and the HAMP-like domain of BceS is shown in Fig. 4a, with the positions
246 of the critical packing points highlighted. The hydrophobicity at these positions is largely
247 conserved in BceS, with the exception of two positions occupied by negatively charged Glu
248 instead. Additionally, the conserved Pro residue in helix 1, and Glu in helix 2, typical for
249 HAMP domains, are not present in BceS (Fig. 4a).

250 Previous investigations of HAMP domains have highlighted one particular residue with key
251 influence on the signaling state, most commonly occupied by small hydrophobic residues that
252 favour bundle packing (Hulko *et al.*, 2006). This residue corresponds to L67 in BceS (Fig. 4a,
253 black arrow). Based on structural work on the HAMP domain of the *A. fulgidus* protein

254 Af1503, this residue (A291 in Af1503) is crucial in controlling the domain's conformational
255 state. Specifically, it is thought that increasing residue size at this position decreases the
256 threshold for conversion between packing states and can cause increased signal
257 responsiveness or elevated kinase activity, while smaller residues decrease activity (Hulko *et*
258 *al.*, 2006; Ferris *et al.*, 2011; Ferris *et al.*, 2012) (Matamouros *et al.*, 2015).

259 To test if the HAMP-like domain in BceS fulfils an equivalent function to *bona fide* HAMP
260 domains, we therefore investigated the role of amino acid size at this position by changing
261 L67 to the smaller Gly and Cys, as well as the larger Phe (Fig. 4b). Indeed, smaller size
262 substitutions reduced BceS activity, up to a near-complete loss of induction in the Gly variant
263 (Fig. 4c). Increasing the size to Phe, however, did not lead to an increase of signaling nor
264 basal activity of BceS. This is consistent with small residues potentially increasing the
265 threshold for conversion between domain conformations (Hulko *et al.*, 2006; Ferris *et al.*,
266 2011), but we could not find a stimulating effect through a larger residue. We nevertheless
267 conclude that the HAMP-like domain in BceS is likely a functional equivalent to
268 conventional HAMP domains in other proteins contributing to signal transfer within the
269 histidine kinase.

270 For further functional investigation, we carried out Cys scanning mutagenesis of the HAMP-
271 like domain. The majority of variants maintained at least partial signaling activity (Fig. S4),
272 and in contrast to other studies (Appleman and Stewart, 2003; Matamouros *et al.*, 2015), we
273 did not find any substitutions that led to constitutive activation. The only two substitutions
274 that caused a complete loss of function were E60C and F63C (Fig. 4 and S4). Interestingly,
275 these fall on the first two positions of the packing motif (Fig. 4a, white arrows and 4d), with
276 E60 located one packing layer above the critical L67 discussed earlier, and are therefore
277 likely of structural importance. Both variant proteins are present in the cytoplasmic

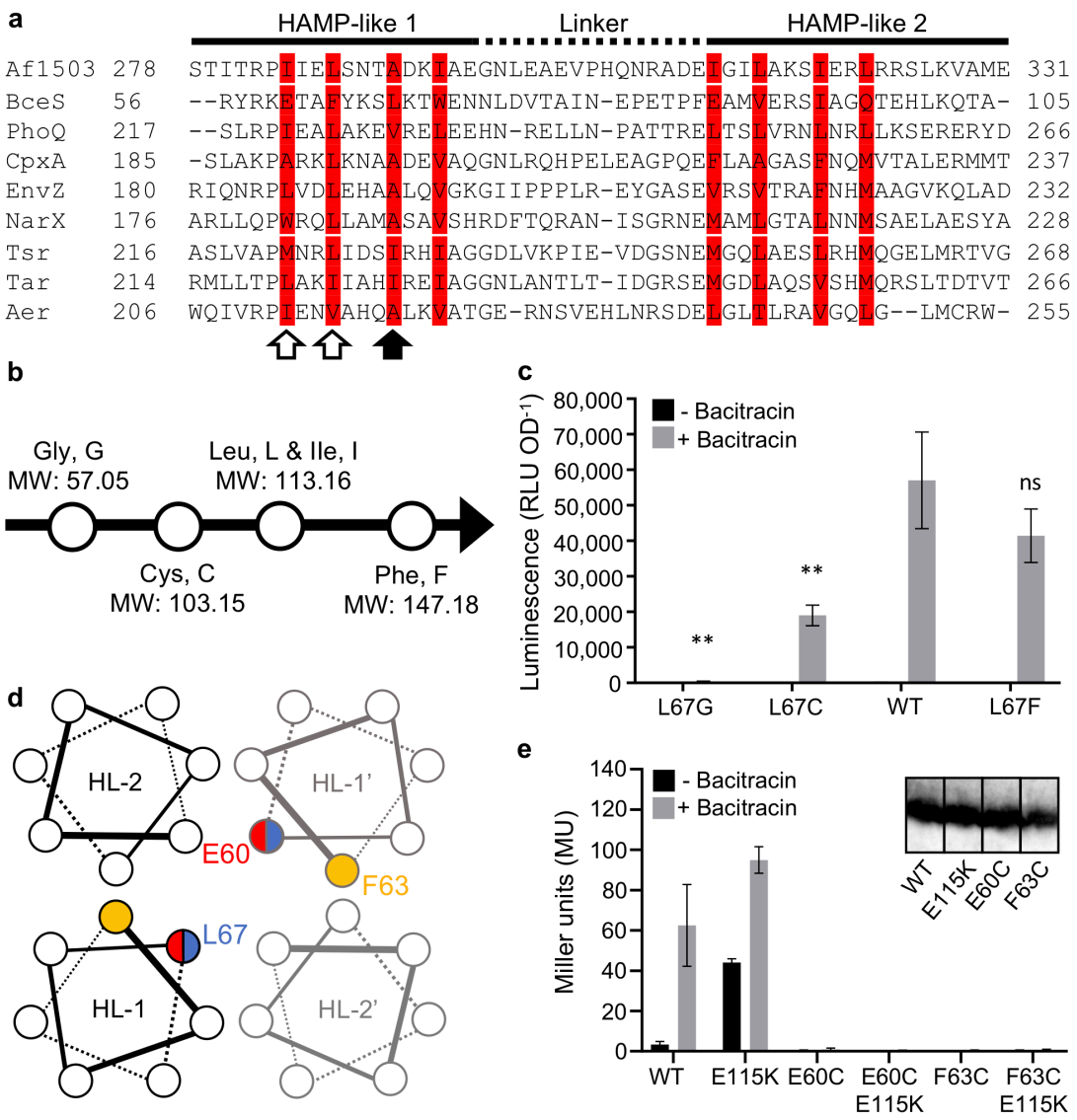

Figure 4: BceS contains a HAMP-like signal transfer domain. a, Sequence alignment of known HAMP domains and the BceS HAMP-like domain generated with ClustalO. Residues in red form the packing layers in the Af1503 HAMP domain. The black solid arrow indicates the packing residue that influences signaling state in some HAMP domains. White open arrows indicate E60 and F63 critical for BceS function. Proteins included and their GenBank identifiers are Af1503 (O28769), BceS (BSU30390), PhoQ (P23837), CpxA (P0AE82), EnvZ (P0AEJ4), NarX (P0AFA2), Tsr (P02942), Tar (P07017), Aer (P50466). b, Schematic showing amino acids and their sizes in MW used in size substitutions. c, BceS signaling activity following L67 amino acid size substitution harbouring PbceA-luxABCDE and Pxyl-bceS. Amino acid substitutions were introduced in the parent construct bceSWT-His8 (SGB369). Signaling was induced with 1µg ml-1 of bacitracin. Data are shown as mean ± SD from 3-18 biological repeats. **, significant difference (p<0.01) in activity compared to WT construct, determined by un-paired t-test; ns, not significant; in the absence of bacitracin, no significant differences were detected. d, Helical wheel diagram of the HAMP-like domain. Individual helices are abbreviated HL-1 and HL-2; the labels HL-1' and HL-2' show the second protomer. Residues essential for BceS activity are E60 (red) and F63 (yellow); the key packing residue L67 is shown in blue; red/blue semicircles are used to indicate positioning of residues in subsequent helical layers. e, BceS signaling activity of the constitutive ON variant (BceSE115K) combined with loss-of-function substitutions at positions 60 and 63. Amino acid substitutions were introduced in parent construct bceSWT-His8 (SGB401). Signaling in cells harbouring PbceA-lacZ and Pxyl-bceS was induced with 1µg ml-1 of bacitracin, BceS production was controlled by addition of 0.02 % (w/v) xylose. Signalling is reported as β-galactosidase activity in Miller units, and data are shown as mean ± SD from 3-7 biological repeats. The inset shows an anti-His Western blot analysis to confirm membrane localisation and protein levels of wild-type (WT) BceS and its variants.

278 membrane at the same levels as the wild type protein according to Western blot analysis (Fig.
279 4e inset), showing that the lack of signaling is not caused by general protein misfolding. To
280 test if the defect of the two variants was due to a loss of signal transfer from either the
281 membrane region of the protein or the transporter, we combined each of the LOF mutations
282 with the E115K substitution that constitutively activates BceS. All resulting variants
283 remained inactive (Fig. 4e), suggesting that the substitutions in the HAMP-like domain likely
284 caused structural disruptions, rather than specifically affecting signal transfer.

285 **Activation of BceS involves a piston-like displacement in transmembrane helix 2.** We
286 next investigated the conformation of the second transmembrane helix in BceS. In many
287 histidine kinases, conformational changes in an extracellular sensory domain are transmitted
288 to the cytoplasmic region through physical movement of the intervening transmembrane helix
289 (Gao and Stock, 2009). In the case of BceS, however, signaling is entirely reliant on the
290 BceAB transport system and therefore does not involve canonical transmembrane
291 information transfer. To investigate if BceS activation nevertheless involved transmembrane
292 helix movements, we carried out a cysteine accessibility scan (Scan-SCAM, (Monzel and
293 Unden, 2015)) of its second transmembrane helix. This analysis requires a cysteine-free
294 background, and we therefore replaced the three native Cys residues mentioned earlier by
295 serine and confirmed that he C45S/C198S/C259S BceS variant was still fully functional (Fig.
296 S5). Individual cysteine replacements were done from positions 51 to 65, surrounding the
297 predicted membrane interface at W54 or F55. The essential residues E60 and F63 were not
298 replaced. All variants were signaling competent (Fig. S5).

299 The position relative to the membrane was then tested for each Cys residue based on its
300 solvent accessibility, using a modified version of the established *E. coli* protocol (Monzel and
301 Unden, 2015). In brief, treatment of whole cells with N-ethyl-maleimide (NEM) should block

302 any solvent-exposed Cys residue, whereas in untreated cells the sulfhydryl groups should
303 remain available for later reactions. Following isolation of membranes, any unblocked Cys
304 residues are then reacted with methoxypolyethylene glycol maleimide (PEG-mal), resulting
305 in a 10 kDa increase in size, detectable by Western Blotting. For cytoplasmic Cys residues in
306 BceS, we therefore expected to see a shift in size only in samples that had not been treated
307 with NEM (Fig. 5, blue labels). In contrast to the established *E. coli* methodology (Monzel
308 and Unden, 2015), we could not observe PEGylation of membrane-embedded Cys residues in
309 *B. subtilis*, regardless of the presence of SDS, possibly due to differences in membrane
310 composition. We therefore interpreted those residues as being membrane embedded that did
311 not show a size shift in either presence or absence of NEM treatment (Fig. 5, red labels).

312 Our results showed that residues up to position 56 resided in the solvent-inaccessible
313 membrane environment, while residues from Y57 onwards were accessible and therefore
314 cytoplasmic (Fig. 5, 'OFF state'). We then repeated the same analysis in the background of
315 the E115K/K116E substitutions that place the kinase in a constitutively active conformation.
316 Here, residues from F55 onwards became consistently solvent-accessible (Fig. 5, 'ON state'),
317 showing that BceS activation involved an inward piston-like displacement by two amino
318 acids of the second transmembrane helix. An interesting observation was residue Y64, which
319 labelled as inaccessible in the OFF state, despite being surrounded by solvent-exposed
320 positions. It is likely that this residue is involved in protein-protein interactions, e.g. within
321 BceS or potentially with BceB, that in the inactive state prevent its labelling through steric
322 effects, as has been proposed before (Monzel and Unden, 2015).

323 We next sought to test whether BceS could be activated by artificially inducing a shift
324 through introduction of positively charged arginine residues near the membrane interface.
325 This approach has been shown to cause signal-independent activation of the *E. coli* histidine

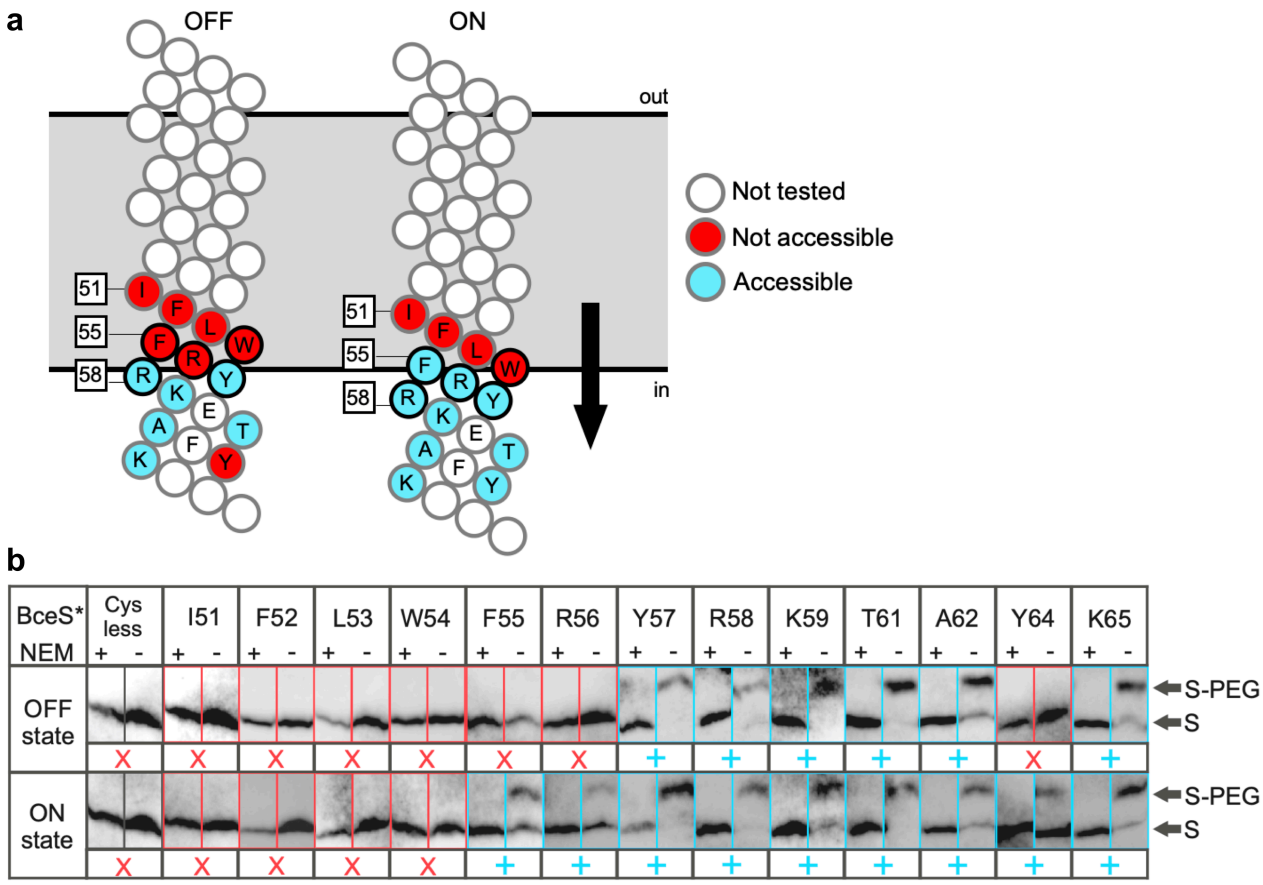

Figure 5: Accessibility of Cys residues at the membrane interface shows a piston-like displacement upon BceS activation. a, Schematic representation of transmembrane helix 2 in the OFF and ON states, respectively. Relevant native amino acids are indicated in one-letter code. Solvent-accessible (PEGylated) Cys replacements are shown in blue, inaccessible (unPEGylated) Cys replacements in red and residues not tested in white. Residues circled in black were tested in triplicate, those circled in grey in duplicate. b, Anti-His Western blot analysis of solvent-accessibility of Cys replacements (Scan-SCAM). Bands corresponding to PEGylated (S-PEG) and unmodified (S) BceS are indicated; individual lanes are outlined in the same colour code as used in panel a. 'Cys-less' indicates the parent variant of BceS lacking its native Cys residues. OFF state: amino acids substituted in parent construct bceSC45S/C198S/C259S-His8 (SGB936). ON state: amino acids substituted in parent construct bceSE115K/K116E/C45S/C198S/C259S-His8 (SGB951).

326 kinase DcuS (Monzel and Unden, 2015). We therefore substituted three of the residues near
327 the cytoplasmic end of transmembrane helix 2 of BceS (W54, F55 and Y57) with Arg,
328 individually and in pairs. (Fig. S6). Variants containing the W54R substitution had
329 approximately 60% higher activities upon stimulation with bacitracin (Fig. S6), which may
330 indicate a stabilisation of or lowered transition threshold to the activated state. However,
331 none of the variants showed a detectable change of basal activity in the presence or absence
332 of the input transporter BceAB, leading us to conclude that Arg substitution alone did not
333 remove the strict reliance on BceAB for signaling.

334 **The transporter BceAB has complete control over kinase conformation**. It was
335 previously shown for several Bce-like sytems that signaling is completely reliant on the
336 transporter (Rietkötter *et al.*, 2008; Ouyang *et al.*, 2010; Staroń *et al.*, 2011; Hiron *et al.*,
337 2011; Gebhard *et al.*, 2014). We further showed through computational modelling that the
338 signaling output via BceS is directly proportional to the activity of BceAB and does not
339 follow the switch-like on/off behaviour seen in most other systems using transporters as
340 accessory sensing proteins (Fritz *et al.*, 2015; Piepenbreier *et al.*, 2017). This led us to
341 hypothesise that BceAB completely controls the conformation of BceS within the sensory
342 complex and thus couples kinase activity directly to its own transport activity. Our discovery
343 of the DHp domain variants that cause artificial activation of BceS now for the first time
344 enabled us to test this hypothesis experimentally by investigating the role of BceAB in
345 controlling the OFF state of the kinase.

346 In cells harbouring the wild-type sequence of BceS, the OFF-state activity was below the
347 detection limit of our assays, and deletion of the transporter therefore had no measurable
348 effect (Fig. 6). However, in the E115K or the E115K/K116E variants, basal kinase activity
349 was high, allowing us to test the effect of *bceAB* deletion in the absence of bacitracin.

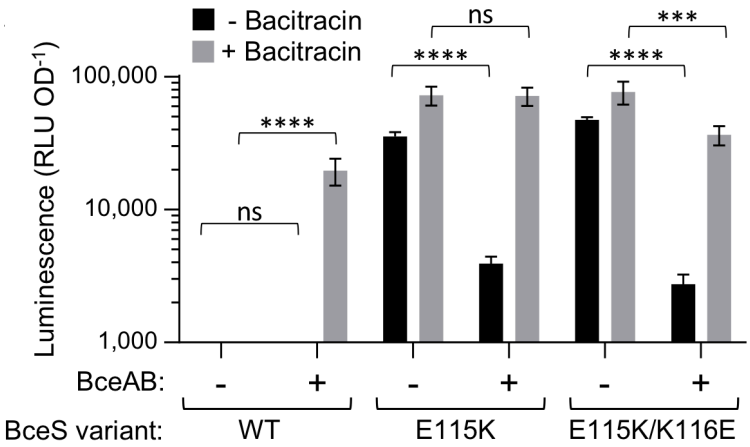

Figure 6: Control of BceS activity by the transporter BceAB. Signaling activity of BceS was measured in strains harbouring PbceA-luxABCDE and challenged with 10µg ml-1 of bacitracin (grey) or left untreated (black). Amino acid substitutions were introduced into parent construct Pxyl-bceS-His8, in a strain background carrying a ΔbceS deletion (BceAB +; SGB792), or a ΔbceSAB deletion (BceAB -; SGB818). Data are shown as mean ± SD from 5-12 biological repeats. Results from unpaired t-test are shown by brackets across the strains and conditions compared, analyzing basal and induced activities separately. ****, $p<0.0001$; ***, $p <0.001$; ns, $p>0.05$. Differences with versus without bacitracin were significant ($p<0.005$) in all strains.

350 Removing the transporter in this background caused a striking further increase in activity,
351 rendering the kinase fully activated irrespective of the presence of the inducing antibiotic
352 (Fig. 6). Therefore, the inactive transporter can inhibit the activity of the constitutively active
353 DHp domain variants approximately ten-fold. Our data are consistent with a model where
354 inactive BceAB exerts close control over BceS keeping the kinase in its inactive state (Fig. 1,
355 left). This reveals a further layer of kinase control in addition to the transporter's known
356 activating effect, e.g. preventing spurious signaling in the absence of antibiotics.

357 **BceAB has not evolved for maximal signaling sensitivity.** Recent structural work has
358 provided new insights into the functional mechanism of the Type VII superfamily of ABC
359 transporters, to which BceAB belongs. They act as mechanotransmitters, using cytoplasmic
360 ATP hydrolysis to provide energy for periplasmic processes, such as removal of antibiotics
361 (Crow *et al.*, 2017). In *E. coli* MacB, mechanotransmission is achieved by the transmembrane
362 helix linking the cytoplasmic ATPase interaction site to the periplasmic domain (Crow *et al.*,
363 2017). In BceAB, the equivalent region is its eighth transmembrane helix (Fig. 1, dark green)
364 (Greene *et al.*, 2018). Based on our earlier discovery that this region of BceB contained a
365 particularly high density of mutations leading to a loss of signaling (Kallenberg *et al.*, 2013),
366 we speculated that this region was crucial for the communication between transporter and
367 kinase. We therefore carried out another Cys scan of residues 533 to 556 in BceB,
368 encompassing approximately half of transmembrane helix 8 and the first alpha-helical
369 segment of the adjacent cytoplasmic region. The native Cys at position 544 was replaced by
370 Ser. Expression of *bceAB* was from a xylose-inducible promoter for consistent transporter
371 production irrespective of signaling activity. The resulting variants, except G535C, displayed
372 comparable bacitracin resistance to the isogenic progenitor strain (Table S2), confirming full
373 functionality of the transporters.

374 Signaling assays showed that all variants except G543C reached a similar amplitude of
375 reporter induction as strains containing the wild-type construct (Fig. S7). However, we
376 observed some clear difference in the sensitivity of signaling, i.e. the minimal concentration
377 of antibiotic required to elicit a response. In cells with the wild-type construct, the lowest
378 bacitracin concentration to trigger signaling was 3 μg ml^{-1}, while a number of variants had a
379 higher threshold of 10 μg ml^{-1} (Fig. 7, green vs pink dots; Fig. S7). The majority of these fell
380 into the C-terminal part of the scanned region, indicating potential defects in coupling to the
381 ATPase. Surprisingly, we found several variants that showed a marked increase in signaling
382 sensitivity and responded already at 0.3 μg ml^{-1} or even 0.03 μg ml^{-1} bacitracin (Fig. 7, dark
383 blue dots; Fig. S7). We had previously seen that a reduction of BceAB transport activity can
384 cause such a shift in signaling threshold, because the negative feedback created by removal of
385 the antibiotic is missing (Fritz *et al.*, 2015). However, as none of these variants showed any
386 change in resistance (Table S2), loss of antibiotic removal cannot explain the increased
387 signaling sensitivity.

388 Residue mapping showed that they occurred with a regular periodicity of every four amino
389 acids (Fig. 7b), suggesting positions along the same face of the transmembrane helix. Figure
390 7c shows a homology model from I-TASSER of the final three transmembrane helices of
391 BceB for illustration. Substitutions with the relatively small amino acid Cys may have
392 enabled tighter helix packing, potentially contributing to more effective signaling. To test
393 this, we replaced two of the positions, L546 and Q550, with a series of other amino acids,
394 including small Ala; charged Glu or Asp; and large Phe. Regardless of the substitution,
395 deviation from the wild-type sequence at these positions consistently led to an increase in
396 signaling sensitivity (Fig. 7b). It is difficult to envisage that all substitutions caused tighter
397 protein interactions. An alternative explanation may be that they are involved in coupling
398 extracellular ligand binding to ATP hydrolysis, and that weakened coupling through the

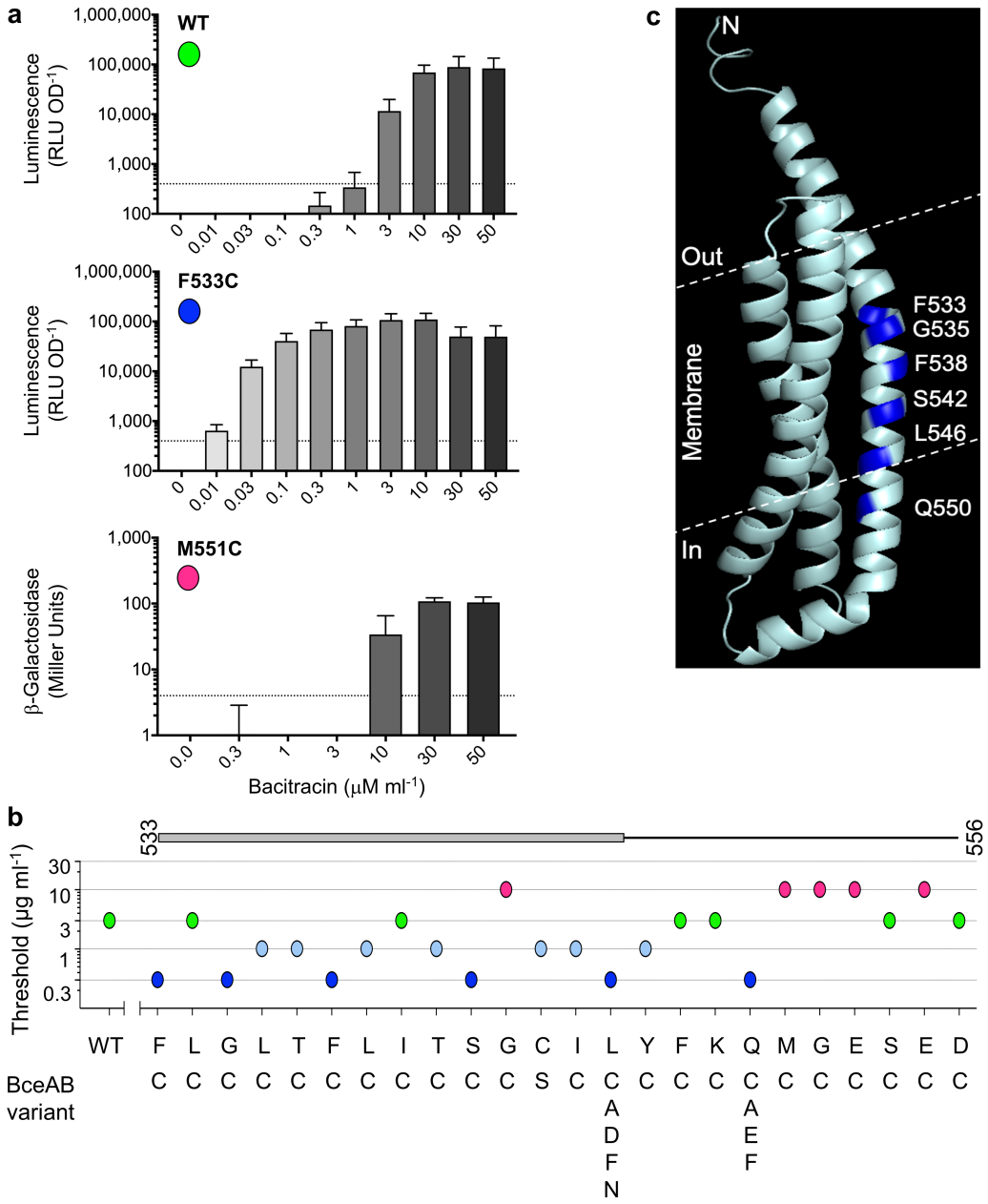

Figure 7: BceAB signals with sub-maximal sensitivity. Amino acid substitutions were introduced into the Pxyl-bceAB-FLAG3 parent construct and signaling assessed using either a PbceA-lacZ (SGB370 and derivatives) or PbceA-luxABCDE (SGB731 and derivatives) reporter. Cells were challenged with a series of bacitracin concentrations for 45 minutes, before signalling activities were determined. a, Signaling phenotype of wild-type (WT) BceAB and representative variants (see Fig. S7 for complete datasets). The colored dots indicate the type of signaling behavior as depicted in panel b (green, WT; blue, hypersensitive signaling; pink, defective signaling). Data are mean ± SD of triplicate experiments. b, Distribution of signaling phenotypes along the transmembrane helix 8 of BceB. The same color symbols are used as in panel a, and the y-axis indicates the threshold bacitracin concentration giving signaling above background. For clarity, threshold concentrations below 0.3 ⍰g ml-1 are not resolved . The first line of x-axis labels gives native amino acids, the lines below indicate substitutions tested. The bar above the graph shows positions in the BceB sequence and areas within the membrane (grey bar) or in the cytoplasm (black line). c, Homology model of the C-terminal three transmembrane helices of BceB (from amino acid 507, C-score -0.66) generated using I-TASSER; the top structural analog was MacB of Acinetobacter baumanii (PDB 5WS4). Positions where amino acid substitutions caused increased signaling sensitivity are highlighted in blue. The approximate predicted membrane boundaries are indicated by a white dashed line.

399 substitutions allowed signaling to occur at lower concentrations. Despite numerous genetic
400 and biochemical attempts, the precise residues with which BceS and BceB interact remain
401 unknown, likely due to an extensive interface between the proteins involving multiple
402 contacts.

403 While it was beyond the scope of this study to pursue a further functional characterization of
404 the transporter, our findings clearly show that BceB contains a series of residues that prevent
405 signaling from occurring at lower bacitracin concentrations. Given that any replacement we
406 tested led to more sensitive signaling, we therefore concluded that evolution of the
407 transporter has actively avoided such hyper-sensitive signaling, constituting a further layer in
408 minimizing the fitness cost of resistance. Under laboratory conditions, we have not yet been
409 able to detect a competitive disadvantage from harbouring hyper-sensitive variants of
410 BceAB. However, fast growth in carefully controlled conditions is not representative of the
411 complex microbial interactions in natural habitats, where energy-conserving regulatory
412 strategies will likely contribute to the competitive success of a microorganism.

413 **DISCUSSION**

414 In this study, we set out to investigate the molecular mechanisms of the flux-sensing strategy
415 employed by Bce-like antibiotic resistance systems. Their hallmark feature is that histidine
416 kinase activity is directly proportional to transport activity across a large input dynamic range
417 of antibiotic concentrations (Fritz *et al.*, 2015). This careful adaptation of signaling ensures
418 the resistance transporter is produced precisely to the cell's demand for detoxification
419 capacity, a very cost-efficient strategy to control gene expression. The results presented here
420 now provide molecular level understanding of how such close control over kinase activity
421 can be achieved.

422 Analyses of BceS conformation in the inactive and active state showed a piston-like inward
423 displacement of the second transmembrane helix upon kinase activation, associated with
424 helical rotation within the DHp domain as inferred from mutagenesis analysis and GaMD
425 simulations. Tertiary structure predictions and experimental validation indicate that BceS
426 possesses an intervening HAMP-like domain that likely fulfils a signal transfer function.

427 While bacterial transmembrane histidine kinases have been studied for decades and we have
428 a very good understanding of the function of the individual domains (reviewed in Gao and
429 Stock, 2009; Jacob-Dubuisson *et al.*, 2018)), a complete understanding of how extracellular
430 events (e.g. ligand binding) are transmitted to the cytoplasmic catalytic domains to trigger
431 autophosphorylation is only beginning to emerge (Gushchin and Gordeliy, 2017; Jacob-
432 Dubuisson *et al.*, 2018). In a canonical transmembrane histidine kinase, extracellular ligand
433 binding causes conformational changes in the sensory domain, which will directly influence
434 the transmembrane segments. Due to the diversity of sensory domains, there is also a
435 diversity in the conformational changes received by the transmembrane helices. In the nitrate
436 sensor NarQ of *E. coli*, for example, nitrate binding by the sensory domain causes a complex
437 combination of a helical break between sensory and transmembrane domains with scissoring
438 and twisting motions at the periplasmic end of the membrane helices. The net result of this is
439 a piston-shift displacement perpendicular to the membrane, which in turn elicits
440 conformational changes in the adjacent cytoplasmic HAMP domain (Gushchin *et al.*, 2017).
441 In the *E. coli* kinases DcuS and CitA, binding of fumarate or citrate, respectively, by an
442 extracellular PAS domain causes compaction of the sensory domain, which displaces the
443 adjacent transmembrane helix towards the periplasm, again resulting in a piston-shift
444 (Monzel and Unden, 2015; Salvi *et al.*, 2017). A piston-shift in the opposite direction, i.e.
445 towards the cytoplasm, is seen in activation of *E. coli* chemoreceptors like Tar (reviewed in
446 Parkinson *et al.*, 2015).

447 Alternative motions in transmembrane signalling are diagonal scissoring displacements, for
448 example in the antimicrobial peptide and cation sensor PhoQ (Molnar *et al.*, 2014), or helical
449 rotations in kinases such as the quorum sensor AgrC of *Staphylococcus aureus* (Wang *et al.*,
450 2014). Due to the diversity of conformational changes, there is currently no consensus model
451 for transmembrane signaling by histidine kinase, and it is likely that the different motions can
452 work together within a single protein (Gushchin and Gordeliy, 2017; Jacob-Dubuisson *et al.*,
453 2018). Our data for BceS suggest that despite its unusual input mechanism via the BceAB
454 transporter, transmembrane signaling is consistent with existing models of kinase activation
455 and occurs via an inward piston displacement. It is of course possible that further structural
456 changes of higher complexity occur in BceS, or indeed within BceS-BceB sensory complex.
457 The unusual behavior of residue Y64 in the Scan-SCAM analyses may provide a first
458 glimpse of such, but this is not currently resolved by our experimental data.

459 To complete signaling and kinase activation, the transmembrane motions will have to be
460 translated into changes within the conserved kinase core to cause autophosphorylation, the
461 common theme for which is helical rotation (Gushchin and Gordeliy, 2017; Jacob-Dubuisson
462 *et al.*, 2018). In kinases where transmembrane signaling already occurs via rotation, the
463 conformational change can likely be directly propagated to the core (Gushchin and Gordeliy,
464 2017). Kinases that signal via piston-displacements, however, require a means of converting
465 this motion into a helical rotation. Recent crystallographic evidence has provided detailed
466 molecular insights into how HAMP domains act as such converters of conformational change
467 (Gushchin *et al.*, 2017). While BceS lacks a *bona fide* HAMP domain, our results are in good
468 agreement with such a mode of signaling, where the piston-shift of transmembrane helix 2 is
469 translated into helical rotations within the DHp domain via the intervening HAMP-like
470 domain.

471 An earlier NMR study reported on the structure of the BceS-like kinase NsaS from *S. aureus*,
472 which possesses a much shorter linker region between its transmembrane and DHp domains
473 (Bhate, Molnar, Goulian, and DeGrado, 2015b). This linker region adopts a coiled-coil
474 conformation instead of the HAMP-like fold of BceS. Inspection of kinase sequences in an
475 existing collection of Bce-like resistance systems (Dintner *et al.*, 2011) showed that the vast
476 majority of these proteins contained the larger version of the linker (approximately 60 amino
477 acids), and only a small number possessed short (around 20 amino acid) linkers with a
478 predicted coiled-coil motif. BceS therefore appears to be the more typical subtype of this
479 group of kinases than NsaS. Interestingly however, akin to the alternative helix packing
480 mechanism proposed for HAMP domains (Hulko *et al.*, 2006), activation of NsaS was also
481 proposed to involve switching between helical packing states of the coiled-coil (Bhate,
482 Molnar, Goulian, and DeGrado, 2015b). The molecular principles of activation may therefore
483 be conserved between both subtypes of BceS-like kinases.

484 To further investigate the activation mechanism of BceS, we sought to force each of the
485 conformational changes via amino acid substitutions. Charge repulsion at the core of the DHp
486 domain to trigger helical rotation consistently led to kinase activation without a physiological
487 stimulus (Fig. 3). However, we were unable to artificially trigger activation through
488 substitutions that should have induced piston displacements in the membrane (Fig. S6) or
489 induced the active conformation of the HAMP domain (Fig. 4 and S4). This is in contrast to
490 studies of other kinases where such substitutions least partially raises the basal activity
491 (Appleman and Stewart, 2003; Matamouros *et al.*, 2015; Monzel and Unden, 2015). In
492 canonical histidine kinases, the input signal is detected directly, e.g. through ligand binding,
493 and it might be speculated that this might be relatively easy to mimic through amino acid
494 substitutions. In contrast, BceS-like proteins are subject to control by the transporter. It is
495 conceivable that in such a kinase small changes in individual domains are insufficient for

496 artificial activation, unless the DHp domain is directly manipulated. This may be supported
497 by the MD simulations, which showed that the wild-type DHp domain does not by itself
498 sample the conformational space observed in the active variant (Fig. S3), implying the
499 transporter may be required to provide the necessary force for transition to the active state.

500 Transporters are commonly used for accessory signaling control, but BceAB is unusual in
501 that it is an activator of signaling, while most others act as repressors (Piepenbreier *et al.*,
502 2017). We previously showed that transporter and kinase constitutively form a signaling
503 complex in the membrane, irrespective of the inducer, bacitracin (Dintner *et al.*, 2014). To
504 activate the kinase proportionally to transport activity, the transporter must therefore be able
505 to directly influence kinase activity within this complex. When we first tested this *in vitro*, we
506 noted that BceAB reduced kinase autophosphorylation in the OFF state, but could not explain
507 the observation at the time (Dintner *et al.*, 2014). Here, we now showed that the transporter
508 indeed not only controls the ON but also the OFF state of BceS (Fig. 6). We propose that
509 through controlling both states of the kinase, the transporter is able to exert the close control
510 needed to explain how signaling is maintained in proportion to transport activity over more
511 than three orders of magnitude in antibiotic concentrations (Fritz *et al.*, 2015). A crucial
512 feature of the flux-sensing mechanism is an immediate reduction of signaling if transport
513 activity is low, either because the antibiotic threat is over or because of sufficient
514 detoxification capacity (Fritz *et al.*, 2015). The active switching off of BceS by BceAB
515 described here explains how this is realized on the molecular level. Complete control also
516 allows the transporter to actively prevent spurious signaling by the two-component system.
517 Finally, our mutagenesis analysis of BceAB revealed that evolution of the transporter itself
518 appears to have actively avoided signaling at very low antibiotic concentrations, highlighting
519 yet another level of cost reduction.

520 Taken together, we here present a molecular level model for activation of antibiotic
521 resistance based directly on the cell's need for protection, using a flux-sensing signaling
522 strategy that employs multiple layers of active energy conservation to minimize fitness costs
523 of resistance. The system is centered on two-component signaling, one of the most important
524 regulatory features of bacteria. Our findings should therefore have wide relevance and serve
525 as a model for understanding how fine-tuned gene expression in bacteria can achieve an
526 optimal cost-benefit balance.

527 **EXPERIMENTAL PROCEDURES**

528 **Bacterial strains and growth conditions.** All strains used in this study are listed in table S1
529 and were routinely grown in Lysogeny Broth (LB; 10 g l^{-1} tryptone, 5 g l^{-1} yeast extract, 5 g l^{-}
530 ^{1} NaCl) at 37 ºC with aeration. Solid media contained 15 g l^{-1} agar. Selective media contained
531 chloramphenicol (5 µg ml^{-1}), macrolide-lincosamide-streptogramin B (erythromycin; 1 µg
532 ml^{-1}, lincomycin; 25 µg ml^{-1}), spectinomycin (100 µg ml^{-1}), kanamycin (10 µg ml^{-1}), or
533 ampicillin (100 µg ml^{-1}).

534 **DNA manipulation and strain construction.** All primers and plasmids used in this study
535 are given in table S1. Site-directed mutagenesis was carried out according to the
536 manufacturer's instructions for the QuikChange II site-directed mutagenesis kit (Agilent
537 Technologies), or by PCR-overlap extension (Ho *et al.*, 1989). *Bacillus subtilis*
538 transformations were carried out via natural competence as previously described (Harwood
539 and Cutting, 1990). DNA for transformation was either provided as linearised plasmid DNA,
540 or as genomic DNA from a *B. subtilis* strain already carrying the desired genetic construct.

541 To allow manipulation of both *bceS* and *bceAB* sequences, an unmarked deletion strain
542 lacking all three genes (Δ*bceSAB*, SGB377) was constructed as described previously (Arnaud

543 *et al.*, 2004), employing plasmid pAK102. Strains lacking *bceS* only (Δ*bceS*; TMB1036) or
544 *bceAB* only (*bceAB*::kan; TMB035 (Rietkötter *et al.*, 2008)) were available from previous
545 work. Signaling activity was assessed in strains harbouring a chromosomally integrated
546 transcriptional reporter construct of the target promoter P_{bceA}, fused to either *luxABCDE*
547 (pSDlux101 (Kallenberg *et al.*, 2013)) or *lacZ* (pER603 (Rietkötter *et al.*, 2008)). Details of
548 the assays used are given below.

549 Genetic manipulation of *bceS* was performed using previously constructed plasmids as
550 template. For Western blot detection, the construct pSD2E01 encoding BceS with a C-
551 terminal octa-histidine tag (P_{xyl}-*bceS*^{WT}-His_8 (Dintner *et al.*, 2014)) was employed. Un-tagged
552 constructs were derived from pAS719 (P_{xyl}-*bceS*^{WT}). Genetic manipulation of *bceAB* was
553 performed using the previously constructed plasmid pFK727, encoding BceAB with a C-
554 terminal triple FLAG-tag on the permease (P_{xyl}-*bceAB*-$FLAG_3$ (Kallenberg *et al.*, 2013)). All
555 constructs used in this study integrate stably and as a single copy into the *B. subtilis* W168
556 chromosome.

557 **Signaling activity assays.** In strains carrying the P_{bceA}-*lacZ* reporter, signaling was assessed
558 following challenge of exponentially growing cells with Zn^{2+}-bacitracin (bacitracin) and
559 measured as β-galactosidase activity (expressed in Miller Units), as described previously
560 (Rietkötter *et al.*, 2008). For strains carrying the P_{bceA}-*luxABCDE* reporter, luciferase
561 activities were assayed using a Tecan® Spark® microplate reader controlled by
562 SparkControl™ V2.1 software. Starter cultures were grown at 37 ºC in 2 ml of LB medium
563 overnight, then diluted 1:1000 into fresh medium before adding 100 µl into 96-well plates
564 (black, clear flat bottoms; Corning®). Samples were grown at 37 ˚C with orbital agitation at
565 180 rpm and allowed to achieve early exponential growth (OD_{600} 0.3 – 0.4), before adding
566 Zn^{2+}-bacitracin to a final concentration of 1 µg ml^{-1} unless otherwise indicated. OD_{600} and

567 relative luminescence units (RLU; integration time 1 s) were measured every 5 min and were
568 background-corrected using values from LB-only wells. RLU was normalised for cell density
569 (RLU OD^{-1}). The reported values are steady-state activities achieved 60-75 min after
570 bacitracin addition.

571 Cells were grown without the addition of xylose, as the basal activity of the promoter P_{xylA}
572 (Radeck *et al.*, 2013), used to drive expression of the ectopic copies of *bceS* and/or *bceAB*,
573 was sufficient to achieve full signaling activity. In strains containing the native copy of
574 *bceAB* (Δ*bceS* background) signaling was induced with 10 µg ml^{-1} of Zn^{2+}-bacitracin. In
575 strains containing only the ectopic construct for BceAB production (Δ*bceSAB* background),
576 signaling was induced with 1 µg ml^{-1} of Zn^{2+}-bacitracin. These concentrations were
577 established in our earlier work as eliciting maximum signaling activity in the respective
578 genetic backgrounds (Fritz *et al.*, 2015).

579 **Bacitracin sensitivity assays.** The sensitivity of *B. subtilis* strains to bacitracin was
580 determined as described (Kallenberg *et al.*, 2013), with minor modifications. Serial two-fold
581 dilutions of Zn^{2+}-bacitracin from 32 µg ml^{-1} to 0.5 µg ml^{-1} were prepared in Mueller-Hinton
582 medium containing 0.2 % (w/v) xylose to ensure maximal production of BceAB. For each
583 concentration, 100 µl volumes in 96-well plates were inoculated 1:400 from overnight
584 cultures grown in Mueller-Hinton medium with xylose and selective antibiotics. Each culture
585 was scored for growth after 20 to 24 h of incubation at 37°C with aeration. The MIC was
586 determined as the lowest bacitracin concentration where no visible growth was detected.

587 **Cysteine cross-linking *in vivo*.** Cysteine cross-linking was assessed in strains carrying the
588 Δ*bceSAB* deletion complemented with xylose-inducible ectopic copies of *bceAB*-$FLAG_3$ and
589 *bceS*-His_8 with single-cysteine substitutions and the P_{bceA}-*lux* reporter (SGB369 and
590 derivatives). Starter cultures were grown in 2 ml of LB medium overnight at 37 ºC with

591 agitation, then diluted 1:500 into 55 ml of fresh medium supplemented with 0.02% (w/v)
592 xylose. In mid-exponential growth (OD_{600} 0.5 – 0.7), oxidative cross-linking of cysteine
593 residues was triggered by addition of 250 µM of iodine for 15 min under continued
594 incubation. Where required, cells were induced with 60 µg ml^{-1} Zn^{2+}-bacitracin for 45 min
595 prior to cross-linking. Cross-linking reactions were stopped with 20 mM N-ethylmaleimide
596 (NEM) for 15 min under continued incubation. Cells were harvested by centrifugation (3,000
597 × *g*, 20 min, 4 ºC) and resuspended in 5 ml of ice cold lysis buffer (100 mM Tris-HCl [pH
598 8.0], 150 mM NaCl, 10% (w/v) glycerol, 20 mM NEM). Cell disruption was achieved by at
599 least three cycles of 15s sonication on ice with 15s rest. Debris was removed by
600 centrifugation (3,000 × *g*, 20 min, 4 ºC), and membranes were collected from supernatants by
601 ultracentrifugation (150,000 × *g*, 1 h, 4 ºC). Membranes were resuspended in 50 µl lysis
602 buffer, and approximately 150 mg protein per sample was mixed with non-reducing sample
603 buffer (1× final concentration; 1.5 M Tris/HCl [pH 6.8], 30 % (w/v) glycerol, 350 mM SDS,
604 0.12 mg ml^{-1} bromophenol blue) for SDS-PAGE and Western blot analysis (see below). For
605 quantification of band intensities Fiji (Schindelin *et al.*, 2012) was used to obtain a profile
606 plot of each lane, and the relative intensity of each band (monomer and dimer BceS) within
607 the lane was expressed as a percentage of the total band intensities.

608 **Solvent-accessibility of Cysteine residues *in vivo* (Scan-SCAM).** For solvent-accessibility
609 tests in the second transmembrane helix of BceS, the Δ*bceSAB* deletion strain, complemented
610 with xylose-inducible ectopic copies of *bceAB*-$FLAG_3$ and *bceS*-His_8 and the P_{bceA}-*lux*
611 reporter was employed. The *bceS* complementation construct was made cysteine-free via
612 C45S/C198S/C259S substitutions, followed by introduction of single cysteines to be tested
613 (strain SGB936 and derivatives). The same was done in the E115K/K116E variant to assess
614 transmembrane topology in the active state (strain SGB951 and derivatives). Cultures were
615 grown to mid-exponential phase as described above. Cells were harvested, washed twice with

616 50 mM HEPES buffer (pH 6.8) and resuspended in 5 ml of the same buffer. Water exposed
617 (i.e. cytoplasmic) cysteine residues were masked with 40 mM N-Ethylmaleimide (NEM) for
618 1.5 h at room temperature with shaking or left untreated. Masking reactions were stopped by
619 three washes in cold (4 ˚C) 50 mM HEPES buffer (pH 6.8). Cells were resuspended in 5 ml
620 of ice cold lysis buffer, sonicated and membranes collected as above. Membranes were
621 resuspended in 40 µl accessibility buffer (50 mM HEPES [pH 6.8], 1.3% (w/v) SDS).
622 Cysteines that had not been masked with NEM in the first step were labelled with 5 mM
623 methoxypolyethylene glycol maleimide (PEG-mal; Sigma-Aldrich) for 1.5 h at room
624 temperature with agitation. The reaction was stopped with 1× LDS sample buffer (Expedeon)
625 and 250 mM DTT and rested for 5 min. PEG-mal accessible and non-accessible BceS were
626 analyzed by Western Blot.

627 **Western blot analysis.** Protein samples (~150 µg) from *in vivo* cross-linking and Scan-
628 SCAM were subjected to SDS-PAGE on RunBlue™ TEO-Tricine SDS mini gel in either
629 Tris-Tricine-SDS (Sigma-Aldrich) or Teo-Tricine-SDS (Expedeon) buffer, run for 50 min at
630 120V. Samples were transferred to polyvinylidene fluoride (PVDF) membranes (Merck
631 Millipore, activated in 100 % (v/v) methanol) in 1 × RunBlue SDS Running Buffer
632 (Expedeon), 20 % (v/v) methanol at 75 mA for 70 minutes using a PerfectBlue™ Sedec™
633 Semi-Dry Electroblotter (Peqlab). Membranes were blocked with 7.5 % (w/v) skimmed milk
634 powder in PBST (137 mM NaCl, 2.7 mM KCl, 10 mM Na_2HPO_4, 1.8 mM KH_2PO_4 [pH7.4],
635 0.1 % (v/v) Tween 20), washed three times in PBST, and incubated with primary antibody
636 (Penta·His Antibody, QIAGEN®, 1:2000 dilution) in 1% bovine serum albumin in PBST for
637 2h at room temperature. Following three washes in PBST, incubation with secondary
638 antibody (Peroxidase-AffiniPure Goat Anti-Rabbit IgG, Jackson ImmunoResearch Europe
639 Ltd, 1:4000 dilution) was carried out in milk-PBST for 1h at room temperature, followed by
640 three final washes in PBST. Detection of proteins was by chemiluminescence using Pierce™

641 ECL Western Blotting Substrate (Thermo Fisher Scientific Inc.) and a Qiagen CCD camera
642 with Fusion software.

643 **Homology Modelling.** Homology models for the BceS HAMP and DHp domains (positions
644 56 to 174), and for the C-terminal domain of BceAB (from position 507) were generated
645 using I-TASSER with default parameters (Zhang, 2008; Yang *et al.*, 2015). The respective
646 homology model with the highest C-score was selected, and the top-ranking structural analog
647 from PDB identified by I-TASSER was noted for reference. For quality control, the resulting
648 homology model for BceS was compared to its closest structural analog, PDB 3RZW, using
649 the TM-align structural alignment programme implemented in I-TASSER (Zhang, 2008;
650 Yang *et al.*, 2015). The obtained TM-score was 0.771 (where >0.5 assumes the same fold),
651 with a root mean square deviation (RMSD) of 1.68 Å between the structurally aligned
652 residues. The homology model was analysed for Ramachandran outliers using MolProbity
653 (Williams *et al.*, 2017). Eight outliers were identified, all within unstructured loop regions of
654 the model: six fall in the loop connecting the two helices in the HAMP-like domain, and two
655 in the loop connecting the DHp domain helices. The homology model was therefore regarded
656 as a plausible representation of the BceS structure, but with some uncertainty in the linking
657 loops between helical segments.

658 **Gaussian-accelerated molecular dynamics (GaMD) Simulations.** A homology model of
659 the cytoplasmic region of BceS consisting of the DHp and ATPase domains was constructed
660 using I-TASSER as before (Zhang, 2008; Yang *et al.*, 2015). The HAMP-like domain was
661 excluded due to low sequence homology with conventional HAMP domains. The
662 approximate orientation of each BceS monomer with respect to one another was predicted
663 based on cysteine cross-linking data (Fig. 2) and further refined using Z-Dock to perform
664 rigid body protein-protein docking (Pierce *et al.*, 2014), with subsequent side chain rotamers

665 optimised using SCWRL4 (Krivov *et al.*, 2009). After MD equilibration of the dimer model
666 (see below), no Ramachandran outliers were present in the loop connecting the DHp domain
667 helices or elsewhere (only Gly262, located in a flexible loop in the ATPase domain, was just
668 outside the 'allowed region'). The N-terminus of the DHp domain of each monomer was
669 acetylated to cap the α-helix and prevent having a positive charge at the termini. ATP was
670 then docked into each ATP binding site using AutoDock Vina (exhaustiveness set to 32)
671 (Trott and Olson, 2010). The generated model of BceS was then manually modified to
672 construct the E115K/K116E variant. All residues were modelled in their standard protonation
673 states, with His108 and His124 singly protonated on the Nδ1 nitrogen, and all other His
674 singly protonated on the Nε2 nitrogen (as indicated by hydrogen bonding networks). Both
675 systems were solvated in an octahedral water box such that no protein/substrate atom was
676 within 10 Å of the box boundaries, with Na^+ or Cl^- counter ions added as necessary to ensure
677 an overall neutral charge. MD simulations were performed using GPU accelerated Amber16,
678 with the ff14SB force field and TIP3P water model used to describe protein and water
679 molecules respectively. Parameters for ATP were taken from a study by Meagher and
680 colleagues (Meagher *et al.*, 2003). Following a minimisation, heating, NVT and NPT
681 equilibration procedure (described below), Gaussian accelerated MD (GaMD) simulations
682 were done in the NVT ensemble at 300 K (Miao *et al.*, 2015), with a boost potential applied to
683 both the total system potential energy as well as the dihedral potential energies (see also
684 GaMD settings in Table S3). To prepare for production GaMD simulations, a 12 ns long
685 conventional MD run was used to obtain maximum, minimum, average and standard
686 deviation of the system potential energies. Following this, a 66 ns long run was used to
687 update the above parameters (updated every 600 ps) to ensure converged GaMD production
688 parameters. Production GaMD simulations were then run for 4 × 500 ns, using different
689 random seeds for each replica. MD simulations were run using a 2 fs time step with the

690 SHAKE algorithm applied to any bond containing a hydrogen atom. An 8 Å direct space
691 non-bonded cut-off was applied with long-range electrostatics evaluated using the particle
692 mesh Ewald algorithm (Darden *et al.*, 1993). Temperature was regulated using Langevin
693 temperature control (collision frequency of 1 ps^{-1}). All MD and GaMD simulations were
694 performed with a 10 kcal mol^{-1} restraint on the Phi and Psi dihedrals between the acetyl and
695 first N-terminal residue, to prevent the α-helix fraying. Principal component analysis (PCA)
696 and other trajectory analyses were performed within CPPTRAJ (Roe and Cheatham, 2013), on
697 the Cα atoms of the DHp domain residues. PCA was performed on the trajectories after
698 constructing an average structure of all four simulations combined. Reweighting of PCA and
699 distance measurements (to obtain PMFs) was performed using the 'PyReweighting' toolkit
700 (Miao *et al.*, 2014).
701 To equilibrate structures for GaMD simulations, the following procedure was performed.
702 Minimisation of all hydrogen atoms and solvent molecules was done using 500 steps of
703 steepest descent followed by 500 steps of conjugate gradient. To keep all other atoms (i.e. the
704 protein heavy atoms) in place during the minimisation, 10 kcal mol^{-1} $Å^{-1}$ positional restraints
705 were applied. Retaining the positional restraints on all protein heavy atoms, the system was
706 then heated rapidly from 50 K to 300 K in the NVT ensemble over the course of 200 ps. This
707 system was again minimised for a further 500 steps of steepest descent followed by 500 steps
708 of conjugate gradient, this time only applying positional restraints (of size 5 kcal mol^{-1} $Å^{-1}$)
709 to the Cα carbon atoms. These Cα restraints were retained as the system was again heated
710 from 25 K to 300 K over the course of 50 ps in the NVT ensemble. Simulations were then
711 performed in the NPT ensemble (1 atm, 300 K), first gradually reducing the 5 kcal mol^{-1} $Å^{-1}$
712 Cα carbon restraints over the course of 50 ps of simulation time. This was done in five steps
713 (5, 4, 3, 2, 1 kcal mol^{-1} $Å^{-1}$) of 10 ps each. A final 20 ns long MD simulation was then
714 performed, in which no restraints were used, to equilibrate the box size. All dynamics steps

715 used the SHAKE algorithm. Simulations performed in the NVT ensemble used Langevin
716 temperature control (with a collision frequency of 1 ps^{-1}) and a simulation time-step of 1 fs.
717 Simulations performed in the NPT ensemble again used Langevin temperature control
718 (collision frequency of 1 ps^{-1}) and a Berendsen barostat (1 ps pressure relaxation time), with
719 a simulation time-step of 2 fs.
720

721 **ACKNOWLEDGEMENTS**

722 The authors thank Roger Draheim for helpful advice in establishing the cysteine crosslinking
723 assays. We also thank our undergraduate research students Jessica Lancaster and Adam
724 McCartan for constructing plasmids pJL705 and pAM703, respectively. We thank Jean van
725 den Elsen and Laurence Hurst for critical reading of and feedback on the manuscript.

726 Work in SG's lab was supported by the Biotechnology and Biological Sciences Research
727 Council (BBSRC; BB/M029255/1). MWK is a BBSRC David Phillips Fellow
728 (BB/M026280/1).

729

730 **AUTHOR CONTRIBUTIONS**

731 AK and MJG carried out all laboratory work and data analysis; MWK and CRP performed
732 and analyzed the MD simulations; SG supervised all laboratory work and coordinated the
733 research project; SG, CRP and AK wrote the manuscript.

734

735 **ABBREVIATED SUMMARY**

One of the main counteracting forces working against the development and spread of antibiotic resistance is the associated cost in fitness, which can be minimized through careful gene regulation. We here investigated fine-tuned signalling via a sensory complex consisting of a transporter and a histidine kinase. We show how the kinase is activated upon antibiotic attack, that the transporter exerts complete control over the kinase, and also has itself evolved to conserve energy.

REFERENCES

Andersson, D.I., and Hughes, D. (2010) Antibiotic resistance and its cost: is it possible to reverse resistance? *Nat Rev Microbiol* **8**: 260–271.

Appleman, J.A., and Stewart, V. (2003) Mutational Analysis of a Conserved Signal-Transducing Element: the HAMP Linker of the *Escherichia coli* Nitrate Sensor NarX. *J Bacteriol* **185**: 89–97.

Arnaud, M., Chastanet, A., and Débarbouillé, M. (2004) New vector for efficient allelic replacement in naturally nontransformable, low-GC-content, Gram-positive bacteria. *Appl Environ Microbiol* **70**: 6887–6891.

Bhate, M.P., Lemmin, T., Kuenze, G., Mensa, B., Ganguly, S., Peters, J.M., *et al.* (2018) Structure and Function of the Transmembrane Domain of NsaS, an Antibiotic Sensing Histidine Kinase in *Staphylococcus aureus*. *J Am Chem Soc* **140**: 7471–7485.

Bhate, M.P., Molnar, K.S., Goulian, M., and DeGrado, W.F. (2015a) Signal Transduction in Histidine Kinases: Insights from New Structures. *Structure/Folding and Design* **23**: 981–994.

Bhate, M.P., Molnar, K.S., Goulian, M., and DeGrado, W.F. (2015b) Signal Transduction in Histidine Kinases: Insights from New Structures. *Structure/Folding and Design* **23**: 981–994.

Crow, A., Greene, N.P., Kaplan, E., and Koronakis, V. (2017) Structure and mechanotransmission mechanism of the MacB ABC transporter superfamily. *Proc Natl Acad Sci USA* **23**: 201712153–6.

Darden, T., York, D., and Pedersen, L. (1993) Particle mesh Ewald: An N·log(N) method for Ewald sums in large systems. *The Journal of Chemical Physics* **98**: 10089–10092.

Dintner, S., Heermann, R., Fang, C., Jung, K., and Gebhard, S. (2014) A sensory complex consisting of an ATP-binding cassette transporter and a two-component regulatory system controls bacitracin resistance in *Bacillus subtilis*. *J Biol Chem* **289**: 27899–27910.

767 Dintner, S., Staroń, A., Berchtold, E., Petri, T., Mascher, T., and Gebhard, S. (2011)
768 Coevolution of ABC transporters and two-component regulatory systems as resistance
769 modules against antimicrobial peptides in Firmicutes bacteria. *J Bacteriol* **193**: 3851–3862.

770 Durão, P., Balbontín, R., and Gordo, I. (2018) Evolutionary Mechanisms Shaping the
771 Maintenance of Antibiotic Resistance. *Trends Microbiol* **26**: 677–691.

772 Ferris, H.U., Dunin-Horkawicz, S., Hornig, N., Hulko, M., Martin, J., Schultz, J.E., *et al.*
773 (2012) Mechanism of Regulation of Receptor Histidine Kinases. *Structure/Folding and*
774 *Design* **20**: 56–66.

775 Ferris, H.U., Dunin-Horkawicz, S., Mondéjar, L.G., Hulko, M., Hantke, K., Martin, J., *et al.*
776 (2011) The Mechanisms of HAMP-Mediated Signaling in Transmembrane Receptors.
777 *Structure/Folding and Design* **19**: 378–385.

778 Fritz, G., Dintner, S., Treichel, N.S., Radeck, J., Gerland, U., Mascher, T., and Gebhard, S.
779 (2015) A new way of sensing: need-based activation of antibiotic resistance by a flux-sensing
780 mechanism. *mBio* **6**: e00975–15.

781 Gao, R., and Stock, A.M. (2009) Biological insights from structures of two-component
782 proteins. *Annu Rev Microbiol* **63**: 133–154.

783 Gebhard, S. (2012) ABC transporters of antimicrobial peptides in Firmicutes bacteria -
784 phylogeny, function and regulation. *Mol Microbiol* **86**: 1295–1317.

785 Gebhard, S., and Mascher, T. (2011) Antimicrobial peptide sensing and detoxification
786 modules: unravelling the regulatory circuitry of *Staphylococcus aureus*. *Mol Microbiol* **81**:
787 581–587.

788 Gebhard, S., Fang, C., Shaaly, A., Leslie, D.J., Weimar, M.R., Kalamorz, F., *et al.* (2014)
789 Identification and Characterization of a Bacitracin Resistance Network in *Enterococcus*
790 *faecalis*. *Antimicrob Agents Chemother* **58**: 1425–1433.

791 Greene, N.P., Kaplan, E., Crow, A., and Koronakis, V. (2018) Antibiotic Resistance
792 Mediated by the MacB ABC Transporter Family: A Structural and Functional Perspective.
793 *Front Microbiol* **9**: 1923–17.

794 Gushchin, I., and Gordeliy, V. (2017) Transmembrane Signal Transduction in Two-
795 Component Systems: Piston, Scissoring, or Helical Rotation? *BioEssays* **40**: 1700197–10.

796 Gushchin, I., Melnikov, I., Polovinkin, V., Ishchenko, A., Yuzhakova, A., Buslaev, P., *et al.*
797 (2017) Mechanism of transmembrane signaling by sensor histidine kinases. *Science* **356**:
798 eaah6345–9.

799 Harwood, C.R., and Cutting, S.M. (1990) *Molecular biological methods for Bacillus*. John
800 Wiley & Sons, Chichester, UK.

801 Hiron, A., Falord, M., Valle, J., Débarbouillé, M., and Msadek, T. (2011) Bacitracin and
802 nisin resistance in *Staphylococcus aureus*: a novel pathway involving the BraS/BraR two-
803 component system (SA2417/SA2418) and both the BraD/BraE and VraD/VraE ABC
804 transporters. *Mol Microbiol* **81**: 602–622.

805 Ho, S.N., Hunt, H.D., Horton, R.M., Pullen, J.K., and Pease, L.R. (1989) Site-directed
806 mutagenesis by overlap extension using the polymerase chain reaction. *Gene* **77**: 51–59.

807 Hsieh, Y.-J., and Wanner, B.L. (2010) Global regulation by the seven-component P_i signaling
808 system. *Curr Opin Microbiol* **13**: 198–203.

809 Hulko, M., Berndt, F., Gruber, M., Linder, J.U., Truffault, V., Schultz, A., *et al.* (2006) The
810 HAMP Domain Structure Implies Helix Rotation in Transmembrane Signaling. *Cell* **126**:
811 929–940.

812 Jacob-Dubuisson, F., Mechaly, A., Betton, J.-M., and Antoine, R. (2018) Structural insights
813 into the signalling mechanisms of two-component systems. *Nat Rev Microbiol* **16**: 1–9.

814 Kallenberg, F., Dintner, S., Schmitz, R., and Gebhard, S. (2013) Identification of regions
815 important for resistance and signalling within the antimicrobial peptide transporter BceAB of
816 *Bacillus subtilis*. *J Bacteriol* **195**: 3287–3297.

817 Kobras, C.M., Piepenbreier, H., Emenegger, J., Sim, A., Fritz, G., and Gebhard, S. (2020)
818 BceAB-Type Antibiotic Resistance Transporters Appear To Act by Target Protection of Cell
819 Wall Synthesis. *Antimicrob Agents Chemother* **64**: 321–15.

820 Krivov, G.G., Shapovalov, M.V., and Dunbrack, R.L. (2009) Improved prediction of protein
821 side-chain conformations with SCWRL4. *Proteins* **77**: 778–795.

822 Lai, R.-Z., and Parkinson, J.S. (2014) Functional Suppression of HAMP Domain Signaling
823 Defects in the *E. coli* Serine Chemoreceptor. *J Mol Biol* **426**: 3642–3655.

824 Letunic, I., Doerks, T., and Bork, P. (2012) SMART 7: recent updates to the protein domain
825 annotation resource. *Nucleic Acids Res* **40**: D302–5.

826 Mascher, T. (2006) Intramembrane-sensing histidine kinases: a new family of cell envelope
827 stress sensors in Firmicutes bacteria. *FEMS Microbiol Lett* **264**: 133–144.

828 Matamouros, S., Hager, K.R., and Miller, S.I. (2015) HAMP Domain Rotation and Tilting
829 Movements Associated with Signal Transduction in the PhoQ Sensor Kinase. *mBio* **6**:
830 e00616–15.

831 Meagher, K.L., Redman, L.T., and Carlson, H.A. (2003) Development of polyphosphate
832 parameters for use with the AMBER force field. *J Comput Chem* **24**: 1016–1025.

833 Miao, Y., Feher, V.A., and McCammon, J.A. (2015) Gaussian Accelerated Molecular
834 Dynamics: Unconstrained Enhanced Sampling and Free Energy Calculation. *J Chem Theory*
835 *Comput* **11**: 3584–3595.

836 Miao, Y., Sinko, W., Pierce, L., Bucher, D., Walker, R.C., and McCammon, J.A. (2014)
837 Improved Reweighting of Accelerated Molecular Dynamics Simulations for Free Energy
838 Calculation. *J Chem Theory Comput* **10**: 2677–2689.

839 Molnar, K.S., Bonomi, M., Pellarin, R., Clinthorne, G.D., Gonzalez, G., Goldberg, S.D., *et*
840 *al.* (2014) Cys-scanning disulfide crosslinking and bayesian modeling probe the
841 transmembrane signaling mechanism of the histidine kinase, PhoQ. *Structure* **22**: 1239–1251.

842 Monzel, C., and Unden, G. (2015) Transmembrane signaling in the sensor kinase DcuS of
843 *Escherichia coli*: A long-range piston-type displacement of transmembrane helix 2. *Proc Natl*
844 *Acad Sci USA* **112**: 11042–11047.

845 Ohki, R., Giyanto, Tateno, K., Masuyama, W., Moriya, S., Kobayashi, K., and Ogasawara, N.
846 (2003) The BceRS two-component regulatory system induces expression of the bacitracin
847 transporter, BceAB, in *Bacillus subtilis*. *Mol Microbiol* **49**: 1135–1144.

848 Ouyang, J., Tian, X.L., Versey, J., Wishart, A., and Li, Y.H. (2010) The BceABRS Four-
849 Component System Regulates the Bacitracin-Induced Cell Envelope Stress Response in
850 *Streptococcus mutans*. *Antimicrob Agents Chemother* **54**: 3895–3906.

851 Pakula, A.A., and Simon, M.I. (1992) Determination of transmembrane protein structure by
852 disulfide cross-linking: the *Escherichia coli* Tar receptor. *Proc Natl Acad Sci USA* **89**: 4144–
853 4148.

854 Parkinson, J.S., Hazelbauer, G.L., and Falke, J.J. (2015) Signaling and sensory adaptation in
855 *Escherichia coli* chemoreceptors: 2015 update. *Trends Microbiol* **23**: 257–266.

856 Piepenbreier, H., Fritz, G., and Gebhard, S. (2017) Transporters as information processors in
857 bacterial signalling pathways. *Mol Microbiol* **104**: 1–15.

858 Pierce, B.G., Wiehe, K., Hwang, H., Kim, B.-H., Vreven, T., and Weng, Z. (2014) ZDOCK
859 server: interactive docking prediction of protein-protein complexes and symmetric multimers.
860 *Bioinformatics* **30**: 1771–1773.

861 Radeck, J., Kraft, K., Bartels, J., Cikovic, T., Dürr, F., Emenegger, J., *et al.* (2013) The
862 *Bacillus* BioBrick Box: generation and evaluation of essential genetic building blocks for
863 standardized work with *Bacillus subtilis*. *Journal of Biological Engineering* **7**: 29.

864 Revilla-Guarinos, A., Gebhard, S., Alcántara, C., Staroń, A., Mascher, T., and Zúñiga, M.
865 (2013) Characterization of a regulatory network of peptide antibiotic detoxification modules
866 in *Lactobacillus casei* BL23. *Appl Environ Microbiol* **79**: 3160–3170.

867 Revilla-Guarinos, A., Gebhard, S., Mascher, T., and Zúñiga, M. (2014) Defence against
868 antimicrobial peptides: different strategies in Firmicutes. *Environ Microbiol* **16**: 1225–1237.

869 Rietkötter, E., Hoyer, D., and Mascher, T. (2008) Bacitracin sensing in *Bacillus subtilis*. *Mol*
870 *Microbiol* **68**: 768–785.

871 Roe, D.R., and Cheatham, T.E., III (2013) PTRAJ and CPPTRAJ: Software for Processing
872 and Analysis of Molecular Dynamics Trajectory Data. *J Chem Theory Comput* **9**: 3084–3095.

873 Salvi, M., Schomburg, B., Giller, K., Graf, S., Unden, G., Becker, S., *et al.* (2017) Sensory
874 domain contraction in histidine kinase CitA triggers transmembrane signaling in the
875 membrane-bound sensor. *Proc Natl Acad Sci USA* **114**: 3115–3120.

876 Schindelin, J., Arganda-Carreras, I., Frise, E., Kaynig, V., Longair, M., Pietzsch, T., *et al.*
877 (2012) Fiji: an open-source platform for biological-image analysis. *Nature Methods* **9**: 676–
878 682.

879 Staroń, A., Finkeisen, D.E., and Mascher, T. (2011) Peptide antibiotic sensing and
880 detoxification modules of *Bacillus subtili*s. *Antimicrob Agents Chemother* **55**: 515–525.

881 Tetsch, L., and Jung, K. (2009) The regulatory interplay between membrane-integrated
882 sensors and transport proteins in bacteria. *Mol Microbiol* **73**: 982–991.

883 Trott, O., and Olson, A.J. (2010) AutoDock Vina: improving the speed and accuracy of
884 docking with a new scoring function, efficient optimization, and multithreading. *J Comput*
885 *Chem* **31**: 455–461.

886 Unden, G., Wörner, S., and Monzel, C. (2016) Cooperation of secondary transporters and
887 sensor kinases in transmembrane signalling: the DctA/DcuS and DcuB/DcuS sensor
888 complexes of *Escherichia coli*. *Adv Microb Physiol* **68**: 139–167.

889 Waglechner, N., and Wright, G.D. (2017) Antibiotic resistance: it's bad, but why isn't it
890 worse? *BMC Biol* **15**: 1–8.

891 Wang, B., Zhao, A., Novick, R.P., and Muir, T.W. (2014) Activation and inhibition of the
892 receptor histidine kinase AgrC occurs through opposite helical transduction motions.
893 *Molecular Cell* **53**: 929–940.

894 Williams, C.J., Headd, J.J., Moriarty, N.W., Prisant, M.G., Videau, L.L., Deis, L.N., *et al.*
895 (2017) MolProbity: More and better reference data for improved all-atom structure
896 validation. *Protein Science* **27**: 293–315.

897 Witan, J., Bauer, J., Wittig, I., Steinmetz, P.A., Erker, W., and Unden, G. (2012) Interaction
898 of the *Escherichia coli* transporter DctA with the sensor kinase DcuS: presence of functional
899 DctA/DcuS sensor units. *Mol Microbiol* **85**: 846–861.

900 Yang, J., Yan, R., Roy, A., Xu, D., Poisson, J., and Zhang, Y. (2015) The I-TASSER Suite:
901 protein structure and function prediction. *Nature Methods* **12**: 7–8.

902 Zhang, Y. (2008) I-TASSER server for protein 3D structure prediction. *BMC Bioinformatics*
903 **9**: 76–8.

904 Zhou, Q., Ames, P., and Parkinson, J.S. (2011) Biphasic control logic of HAMP domain
905 signalling in the *Escherichia coli* serine chemoreceptor. *Mol Microbiol* **80**: 596–611.

906